CHAPTER 8

STATIC AND SEISMIC LATERAL EARTH PRESSURES FOR RETAINING WALL BACKFILLED WITH UNSATURATED SOIL UNDER STEADY-STATE FLOW

8.1 INTRODUCTION AND REVIEW OF EXISTING STUDIES

The present chapter focuses on determining lateral earth pressures developed in retained unsaturated horizontal and inclined backfills subjected to static and seismic forces during steady state flow condition. Determination of earth pressure of retained soil backfill is a classical problem in geotechnical engineering. Coulomb (1776) and Rankine (1857) pioneered the development of the earth pressure theories way back in the eighteenth and nineteenth centuries. Since then, a good number of researches were carried out to estimate the earth pressures with the help of various analytical and numerical techniques. In most of the previous studies, the soil backfill was typically considered to be either completely dry or completely saturated. However, in reality, most of the backfill soils remain in a partially saturated state. In the last two decades, a few works were carried out on unsaturated soil backfill by using the limit equilibrium method (Pufahl et al. 1983; Lu and Likos 2004; Lu et al. 2010;Zhang et al. 2010; Liang et al. 2012; Vahedifard 2015; Sahoo and Ganesh 2017; Deng and Yang 2019; Abdollahi et al. 2021; Ganesh et al. 2022; Li and Liu 2023), upper bound rigid block method (Zhao et al. 2009; Stanier and Tarantino 2010; Shwan et al. 2016; Li and Yang 2018, Xu et al. 2021; Zhang et al. 2023), finite element limit analysis (Fathipour et al.2020), and displacement-based finite element method (Griffiths and Lu 2005). Most of these studies were performed to evaluate seismic earth pressures on horizontal unsaturated soil backfill with the aid of the closed-form suction stress (σ^s) expression for steady-state water flow (Section 6.2.2). Traditionally, the asymmetry parameter of the vG-SWCC model, m, is assumed to be completely dependent on the n value through the following definite relationship: $m=1-1/n$. This constraint is required to obtain the closed-form solution of the integral form of Mualem's HCF model and implementation of this constraint eventually reduces the number of fitting parameters from three to two. The impact of m on the SWCC curves is well explained in the work of Fredlund et al. (1995). The parameter m governs the asymmetry of the SWCC curve and it provides greater flexibility in fitting SWCC data, especially in the higher matric suction zone. Moreover, m and n parameters retrieved from the SoilVision database (Fredlund and Rahardjo 1993) suggest that this empirical expression does not represent most of the experimental results. Hence, by providing a constraint on the m parameter, the estimation of the stability parameters is compromised to a significant extent.

In addition to the dependence of m parameter, past studies also show that the expression of matric suction is derived by taking Gardner's one-parameter hydraulic conductivity function (HCF) (Eq. 6.10) into account. Although the one-parameter HCF model yields a simplified formulation for a closed-form solution, however, the expression does not consider the impact of desaturation rate on the hydraulic conductivity. No literature, however, seems to be available for estimating the earth pressures on the retaining wall by duly relaxing the constraints imposed on m and considering the HCF to be dependent on the air entry value as well as on the pore size distribution. The first section of this chapter deals with this issue by reformulating the conventional expression of the suction stress, and reexamining the earth pressure in unsaturated backfills based on the newly-developed suction stress expression. This investigation is performed on the vertical wall with horizontal backfilling by employing the modified Rankine's earth pressure theory.

The second segment of this chapter assesses the active earth pressure within inclined backfills which are under variably saturated condition. These backfills are subjected to seismic forces, and are held in place by inclined retaining walls. With the aid of modified Coulomb's earth pressure theory, an extensive investigation is carried out to understand the combined effect of soil's hydro-mechanical properties, GWT location, wall inclination, backfill inclination, steady-state flow characteristics (rate and direction), and seismic forces on the computed active earth pressure. The pseudo-static method is used to realize the action of seismic forces (horizontal and vertical).

8.2 MODIFICATION AND APPLICATION OF RANKINE'S METHOD FOR ADDRESSING VERTICAL RETAINING WALL SUPPORTING UNSATURATED BACKFILL WITH HORIZONTAL SURFACE

8.2.1 Construction of Rankine's based closed-form expression for unsaturated backfills

8.2.1.1 Computation of earth pressure (EP) coefficients

The consideration of vertical retaining wall with horizontal backfilling ensures that the principal planes for any chosen points are aligned in horizontal and vertical directions.Therefore, according to the generalized linear Hookean elasticity, the stress-strain relationship for a homogenous, isotropic, unsaturated soil material can be written as under:

$$\begin{Bmatrix} \varepsilon_1 \\ \varepsilon_2 \\ \varepsilon_3 \end{Bmatrix} = \frac{1}{E} \begin{bmatrix} 1 & -\mu & -\mu \\ -\mu & 1 & -\mu \\ -\mu & -\mu & 1 \end{bmatrix} \begin{Bmatrix} \sigma_1' \\ \sigma_2' \\ \sigma_3' \end{Bmatrix}; \text{ where, } \begin{Bmatrix} \sigma_1' \\ \sigma_2' \\ \sigma_3' \end{Bmatrix} = \begin{Bmatrix} \sigma_1 - u_a - \sigma^s \\ \sigma_2 - u_a - \sigma^s \\ \sigma_3 - u_a - \sigma^s \end{Bmatrix} \qquad (8.1)$$

Considering the plane strain nature of the problem, the normal and shear strains along the wall length become zero, and thus the stress becomes completely dependent on its orthogonal counterpart. Fig. 8.1a shows the three chosen stress points for which the Mohr failure circles are represented in Fig. 8.1c. The Mohr circles are drawn for the no-flow condition subjected to the rest, active and passive failure state. One can observe how the yield circles' size and the yield envelopes' location vary as the concerned point moves closer to the ground surface. For any stress state, the Mohr circle representing the point adjacent to the water table (Point 1) is larger than the Mohr circle representing the point adjacent to the ground surface (Point 3). The formulations of EP coefficients for modified Rankine's earth pressure theory are mentioned below,

8.2.1.1.1 *At Rest State*

When the soil is at rest condition, there would not be any horizontal deformation (i.e., ε_h=0), and hence, the vertical and the horizontal stresses can be related as under:

$$\varepsilon_h = \frac{\sigma_h - u_a}{E} - \frac{\mu}{E}(\sigma_v - u_a + \sigma_h - u_a) + \frac{(1-2\mu)\sigma^s}{E} = 0 \tag{8.2a}$$

$$\Rightarrow \sigma_h - u_a = \frac{\mu}{1-\mu}(\sigma_v - u_a) - \frac{(1-2\mu)\sigma^s}{1-\mu} \tag{8.2b}$$

Therefore, the coefficient of earth pressure at rest condition in the vadose zone (K_{0u}) can be expressed as:

$$K_{0u} = \frac{\sigma_h - u_a}{\sigma_v - u_a} = \frac{\mu}{1-\mu} - \frac{1-2\mu}{1-\mu}\frac{\sigma^s}{\left(\sigma_v - u_a\right)} \quad (\mu = \text{the Poisson's ratio}=0.35) \tag{8.2c}$$

8.2.1.1.2 *At Active State*

Following Rankine's classical theory, the active earth pressure (AEP) coefficient, as modified by Lu and Likos (2004) on the basis of the suction stress concept, is stated as follows:

$$\sigma_h - u_a = \underbrace{\underbrace{\overset{\text{Compressive stress}}{K_a(\sigma_v - u_a)}}_{\substack{\text{AEP due to}\\ \text{Self-weight}}} - \underbrace{\overset{\text{Tensile stress}}{2c'\sqrt{K_a}}}_{\substack{\text{Cohesion}\\ \text{induced AEP}}}}_{\substack{\text{AEP components}\\ \text{for Saturated Soil}}} - \underbrace{\underbrace{\overset{\text{Tensile stress}}{\sigma^s\left(1-K_a\right)}}_{\substack{\text{Suction Stress}\\ \text{induced AEP}}}}_{\substack{\text{Additional AEP}\\ \text{component for Unsat Soil}}} \quad ; K_a = \frac{1-\sin\phi'}{1+\sin\phi'} \tag{8.3a}$$

$$K_{au} = \frac{\sigma_h - u_a}{\sigma_v - u_a} = K_a - \frac{2c'\sqrt{K_a}}{\sigma_v - u_a} - \frac{\sigma^s}{\sigma_v - u_a}\left(1-K_a\right) \tag{8.3b}$$

The failure occurs due to the combined effect of weight force (self-weight of the retained backfill) and the tensile force (cohesion and the matric suction). The vertical and the horizontal stresses are the major and the minor principal stresses, respectively. Fig. 8.1c shows the AEP components arise due to self-weight, cohesion, and suction stress. Like the rest state, thesuction stress generates further tensile stress in the variably saturated zone.

8.2.1.1.3 *At Passive State*

The passive earth pressure (PEP) for homogenous, cohesive-frictional, unsaturated soil can also be calculated by employing Rankine's earth pressure theory and Lu and Likos's (2004) suction stress concept. The passive earth pressure and its coefficient are stated below:

$$\sigma_h - u_a = \overbrace{\underbrace{\underbrace{K_p(\sigma_v - u_a)}_{\substack{\text{PEP due to}\\ \text{Self-weight}}} + \underbrace{2c'\sqrt{K_p}}_{\substack{\text{Cohesion}\\ \text{induced PEP}}}}_{\substack{\text{PEP components}\\ \text{for Saturated Soil}}} + \underbrace{\underbrace{\sigma^s\left(K_p - 1\right)}_{\substack{\text{Suction Stress}\\ \text{induced PEP}}}}_{\substack{\text{Additional PEP}\\ \text{component for Unsat Soil}}}}^{\text{Compressive Stress Components}} \quad ; \ K_p = \frac{1+\sin\phi'}{1-\sin\phi'} \tag{8.4a}$$

$$K_{pu} = \frac{\sigma_h - u_a}{\sigma_v - u_a} = K_p + \frac{2c'\sqrt{K_p}}{\sigma_v - u_a} + \frac{\sigma^s}{\sigma_v - u_a}\left(K_p - 1\right) \tag{8.4b}$$

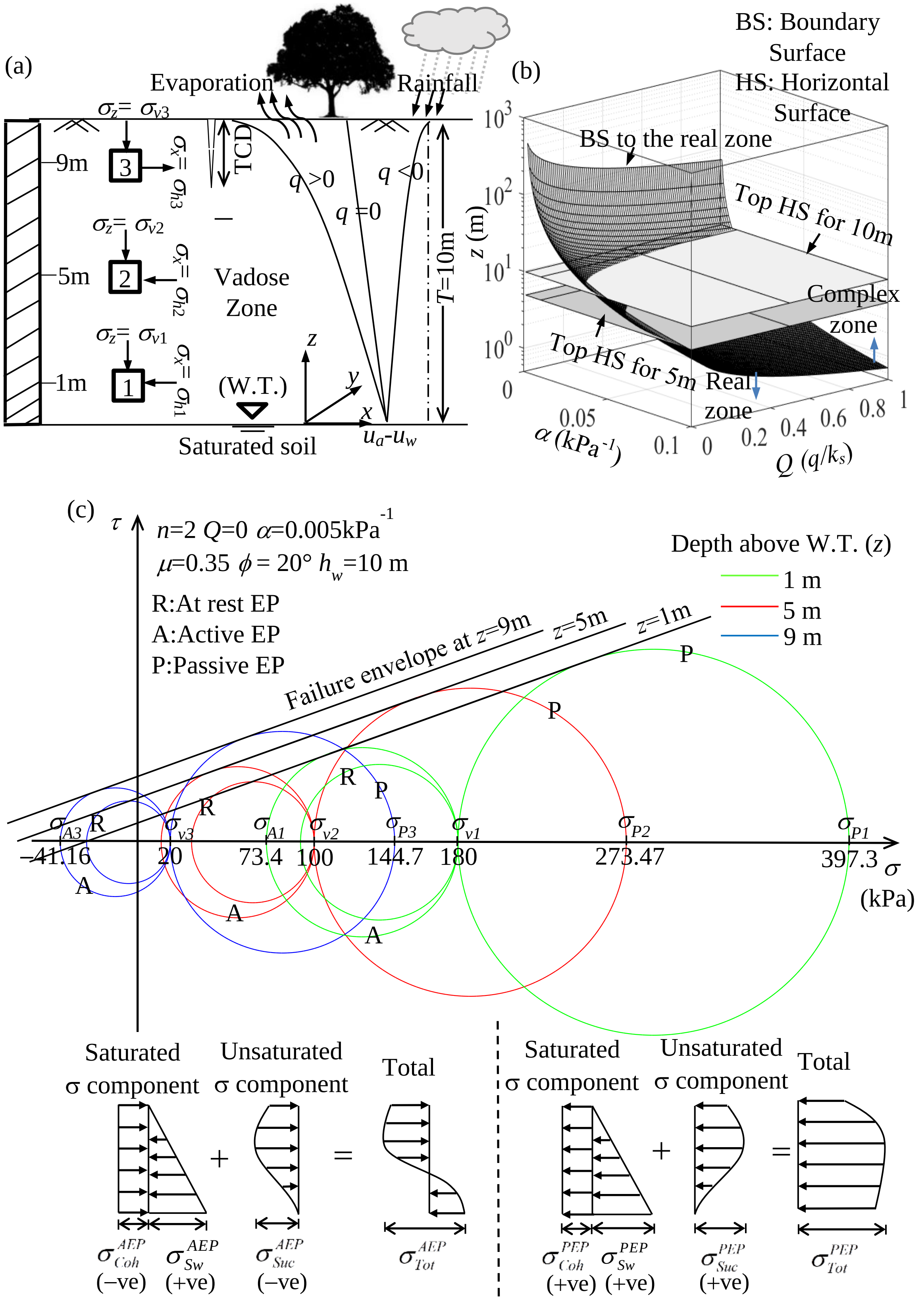

Coh: Cohesion; *Sw*: Self Weight; *Suc*: Suction; *Tot*: Total

AEP and *PEP*: Active Earth Pressure and Passive Earth Pressure resp.

Fig. 8.1 (a) Schematic representation of unsaturated soil-backfill with matric suction variation (b) bounded surface in three-dimensional semi-logarithmic α–Q–z space demarcating the real and the complex zones (c) Mohr-Coulomb failure circles and corresponding failure envelopes along with the components of active and passive stress state distribution.

For soil subjected to active and passive limit states, the failure planes form a group of parallel lines that make an angle of 45°+$\phi'/2$ and 45°−$\phi'/2$ with the horizontal surface, respectively. However, contrary to the active condition, the directions of the principal stresses are reversed in the passive state. Due to the suction stress component, the PEP increases and has non-linear profiles as shown in Fig. 8.1c.

It is noteworthy that irrespective of any stress state, barring the last term, the expression of the EP coefficient is exactly the same for the saturated soil. The last terms involve the effect of matric suction which varies non-linearly with depth, as mentioned in the previous section. Therefore, unlike the saturated soil where the EP coefficient is constant throughout the depth, the suction stress-dependent total EP in the vadose zone generates curvilinear profiles. It is further to be noted that apart from the suction stress and vertical overburden stress, K_{0u} depends on μ, whereas, K_{au} and K_{pu} are the functions of the soil shear strengths ($c'$and ϕ').

8.2.1.2 Computation of tensile crack depth

Eqs.8.2c and 8.3b suggest that the incorporation of matric suction gives rise to additional tensile stress at rest and in active-state conditions. As soil is relatively weak in tension, therefore, tension cracks are likely to develop when the tensile strength is completely mobilized. The tensile crack depth (TCD) is, therefore, worked out by equating the corresponding earth pressure coefficients to zero.

At rest condition: K_{0u} =0 implies, $TCD = \dfrac{1-2\mu}{\mu\alpha\gamma_b}\sigma^s$ (8.5a)

At active state condition: K_{au} =0 implies, $TCD = \dfrac{2c'}{\gamma_b\sqrt{K_a}} + \dfrac{\sigma^s}{\gamma_b}\left(\dfrac{1}{K_a}-1\right)$ (8.5b)

γ_b is the bulk unit weight of the soil. The term $(1\text{-}2\mu)/\mu$ represents the deformability of the soil. It appears that similar to the earth pressure coefficients, TCD depends on the hydromechanical properties (SWCC model parameters, strength parameters, soil unit weight, permeability function), environmental aspects (e.g., flow conditions, water table depth) as well as the vadose zone thickness and can be obtained from Eqs. 8.5a and 8.5b. However, these expressions are implicit and highly non-linear. Hence, they are solved by using the Newton-Raphson iterative technique. The numerical simulations are performed by writing a suitable code in Matlab (R2015a Version).

8.2.2 Strategy for relaxing *m*-parameter and incorporating two-parameter dependent HCF

The suction stress (Eq. 6.11) for steady state flow is derived by combining thevG-SWCC model-based effective degree of saturation (Eq. 6.5b) and Gardner's (1958) one-parameter HCF-based matric suction (Eq. 6.10). Therefore, the spatially varying suction stress explicitly depends on the vG-SWCC model parameters (α, n) and the dimensionless flow ratio ($Q=q/k_s$).

Two of the most commonly used statistical HCF model, namely, Burdine's model (1953) and Mualem's model (1976) evoke the following R_M and R_B terms (as shown in Appendix B), respectively, which relates the m and n parameters unrestrictedly (van-Genuchten and Nielsen 1985). The expressions of R_M (Eq. B.1) and R_B (Eq. B.2) are depicted in Appendix-B.

Conventionally, these terms are taken to be zero. Fig. 8.2a shows how the relationship between m and n changes for different values of R_M and R_B. Similar to the Section 6.2.2, the parameters are widely varied to accommodate a large set of (m, n) pairs. For each n, the set of m values chosen in the analysis is clearly marked in Fig. 8.2a.

Further, in order to investigate the impact of the pore size-dependent HCF model, the following Gardner (1958)'s two parameters hydraulic conductivity model (TPM) is employed:

$$k(\psi) = \frac{k_s}{1 + \alpha\psi^{\xi}} \tag{8.6}$$

Here, ξ is the fitting parameter. Fig. 8.2b shows the variation of permeability function for different values of ξ and two α's, namely, α =0.005 and α =0.01. It can be inferred from the graph that the parameter ξ not only governs the steepness of the HCF curves but also plays a significant role in controlling the ψ at which the curves bent the most. By equating Eqs. (6.10) and (8.6) the expression of ξ is obtained as under:

$$\xi = \frac{\ln\left(\dfrac{\exp(\alpha\psi) - 1}{\alpha}\right)}{\ln\psi} \quad , \psi > 0 \tag{8.7}$$

Corresponding to α=0.005 kPa^{-1}, 0.01 kPa^{-1}, and 0.1 kPa^{-1}, the variation of ξ with respect to ψ is shown in Fig. 8.2c. The solutions from TPM and OPM are exactly the same if the variation of ξ with ψ is suitably adopted in the analysis.

8.2.3 Problem statement and involved assumptions

As shown in Fig. 8.1a, a wall of height, *H*, retains a homogeneous and isotropic cohesive frictional soilbackfill. The water table is assumed to lie at the toe of the retaining wall. The zone below and above the water table is wholly and partially saturated. The saturation state of the retained soil above the water table exhibits a significant variation because of the change in climatic conditions (e.g., rainfall, drought, flooding), vegetation, evapotranspiration, compaction during construction, watering, groundwater table fluctuation, and other natural and anthropogenic factors. The assumptions of fluid flow condition in the backfill are similar to the Section 6.2.

The osmotic, electrical, thermal, and velocity heads are considered negligible, and the hydraulic gradient solely acts as the fundamental driving potential for the water flow. The rest, active and passive earth pressures are computed by considering the modified Mohr–Coulomb failure criterion. The variation of suction stress above the water table is obtained with the help of the vG SWCC model and Gardner's HCF model. The hydraulic head at the water table surface is taken to be zero, and the top ground surface is modelled by employing the flux boundary condition. Moreover, the fluid pressure and the flow rate inside and outside the tension cracks are the same.

It is intended to determine the earth pressures and the tensile crack depth developed in the retained backfill by considering the independence of *m* parameter in the SWCC model and the twoparameter-dependent HCF model. The analysis is carried out for different values of SWCC parameters (α, n, R_M and R_B), flow rates and directions (i.e., infiltration, evaporation, and no-flow conditions), and Gardner's one as well as two-parameter HCF models.

8.2.4 Results and discussions

Considering past literature (Lu and Likos 2004; Vahedifard et al. 2015; Abdollahi et al. 2021), an extensive parametric study is carried out to cover the wide possible ranges of parameters in the field. Irrespective of the SWCC parameters, all soils are considered to have the same shearing strength (c'= 7 kPa, ϕ'= 20^{o}, γ_b =18 kPa) in the completely saturated state. The α-parameter ranges from 0.001kPa^{-1} to 0.5 kPa^{-1} and n is chosen between 2.5 to 8.5. For each n, wide values of m are chosen. The combinations of various m and n used in this manuscript are shown in Fig. 8.2a. It is noteworthy that it is the flow ratio that directly impacts the suction stress and subsequently the earth pressure profiles.

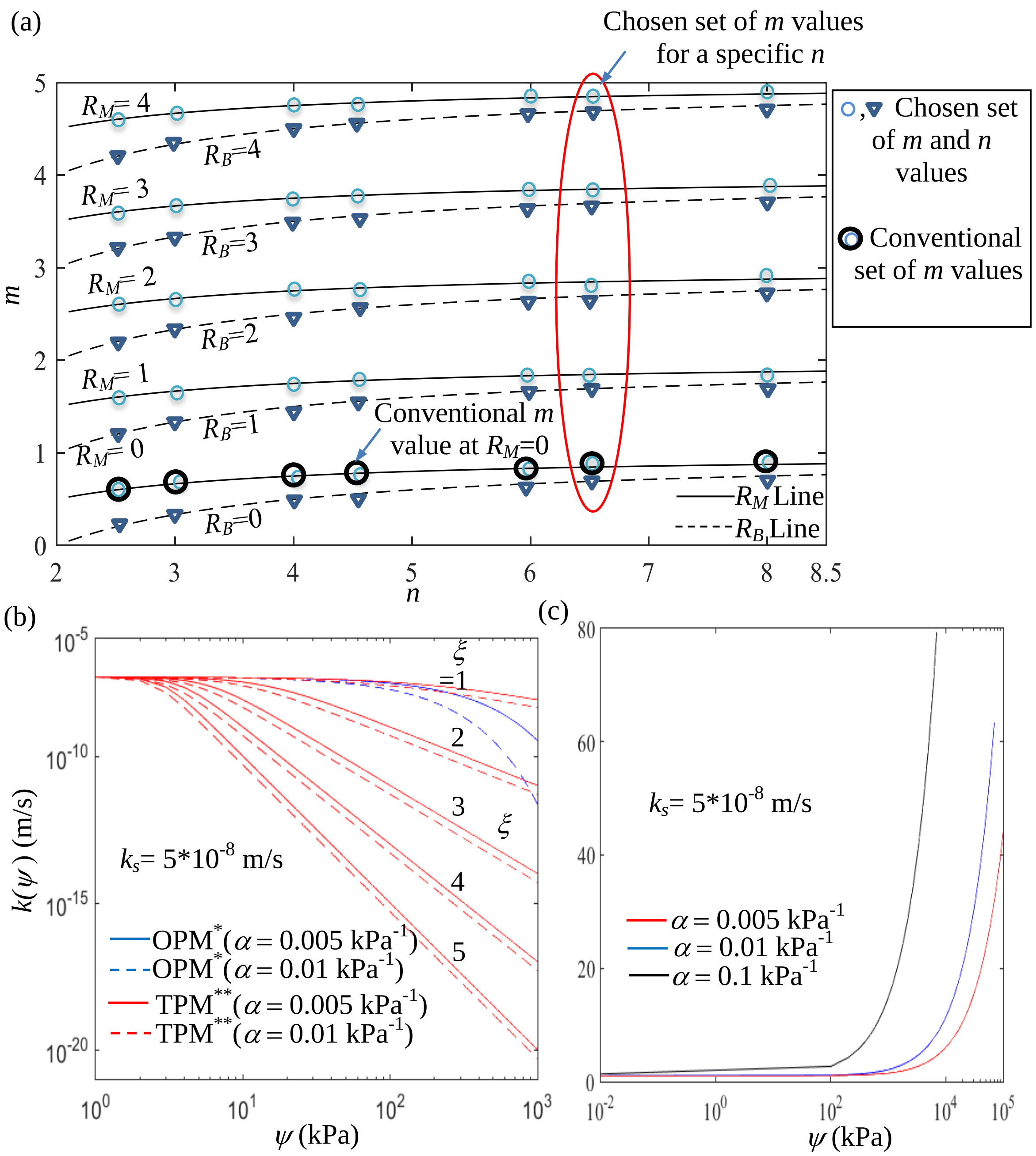

Note:*OPM= Gardener's one parameter model, **TPM= Gardener's two parameter model

Fig. 8.2 (a) The combined set of m and n parameters chosen in the analysis, (b) schematic representation of Gardner's one-parameter and two-parameter HCF models, and (c) variation of ξ for ensuring the similarity between OPM and TPM.

The flow ratios of –0.8, 0, and 0.8 are chosen to investigate the effect of flow rates and directions under extreme conditions. In one of the analyses, the sands and clays are distinctly marked with mentioning the proper k_s values (k_s = 5 x 10^{-4} m/s and 5 x 10^{-8} m/s) with the specific flow rates, e.g., q = –3.14 x 10^{-8} m/s (infiltration), q = 0 (no-flow), and q = 1.15 x 10^{-8} m/s (evaporation), respectively. It can be inferred from Eq. (6.11) that the matric suction and suction stress will be real-valued solutions if the quantity within the logarithmic is positive. Mathematically, it can be expressed as:

$$(1+Q)\exp(-\gamma_w \alpha\, z)-Q>0 \Rightarrow z<\frac{1}{\gamma_w \alpha}\ln\left(\frac{1+Q}{Q}\right) \tag{8.8}$$

Based on α and Q, Fig. 8.1b shows the limiting boundary surface in three-dimensional space which separates the backfill zones into two zones- the real zone and the complex zone. For 5m and 10m retaining walls, the real zone and complex zone are distinctly marked in the figure.

8.2.4.1 Impact of *m* parameter

8.2.4.1.1 *Variations of K_{0u}, K_{au} and K_{pu} for defined k_s*

Fig. 8.3 depicts the variations of K_{0u}, K_{au} and K_{pu} above the water table for sands and clays subjected to three different flow conditions and corresponding to various m and n relations. The following observations are made:

(a) R_M and R_B lines pertaining to K_{0u} are quite distinct for sands as well as for clays. However, the impact of m parameter on the K_{au} and K_{pu} profiles seems to be negligible for sandy soils.

(b) K_{0u} and K_{au} profiles corresponding to sandy soils hardly get perturbed by the variation of flow directions or magnitudes. Nevertheless, the wetting-induced K_{pu} profiles of sands remain slightly above the K_{pu} profiles generated from drying or hydrostatic condition.

(c) Adjacent to the water table, K_{0u} decreases sharply with z. At some z, the curves attain a minimum value ($K_{0u,min}$); thereafter, the trend of the curve changes abruptly and reaches a constant value of saturated K_0. The figure gives an impression that except for a narrow band near the water table surface, the EP coefficient at the no-deformation state is completely independent of suction stress corresponding to sandy soils. For a high value of m, the magnitude of $K_{0u,min}$ decreases, and the location of $K_{0u,min}$ approaches towards the water table. For instance, the peak K_{0u} is attained at z = 1 m and 0.53 m, corresponding to R_M equals to 0 and 4, respectively.

(d) Unlike the coarser soils, the flow conditions impact the EP profiles of fine-grained soils to a noticeable extent. The wetting-induced EP profiles are identical whatsoever be the values of m parameters and remain above all the curves. The impact of m parameter is moderately visible for the hydrostatic condition and the variation of the EP profiles becomes widespread during the drying phase. Unlike sands, tensile cracks are developed in clayey soils even when the clays are subjected to the rest state.

(e) Corresponding to hydrostatic and evaporative situations, the depth at which the EP profiles touch the zero-line (i.e. EP = 0) becomes more profound with the increase in the magnitude of the asymmetry parameter of SWCC curves.

8.2.4.1.2 *Variations of K_{0u}, K_{au}, and K_{pu} for specific Q*

Figs. 8.4, 8.5 and 8.6 demonstrate the variation of EP coefficients corresponding to various (i) m and n relations (R_M and R_B =0, 1, 2, 3, and 4), (ii) three specific flow ratios (Q= 0, ±0.4), (iii) two pore-spectrum numbers (n=2 and 6), and (iv) two different AEV (α =0.1 and 0.005 kPa^{-1}); Fig. 8.4 subscribes to K_{0u}, Figs. 8.5 and 8.6 pertain to K_{au} and K_{pu}, respectively. The following observations are noted:

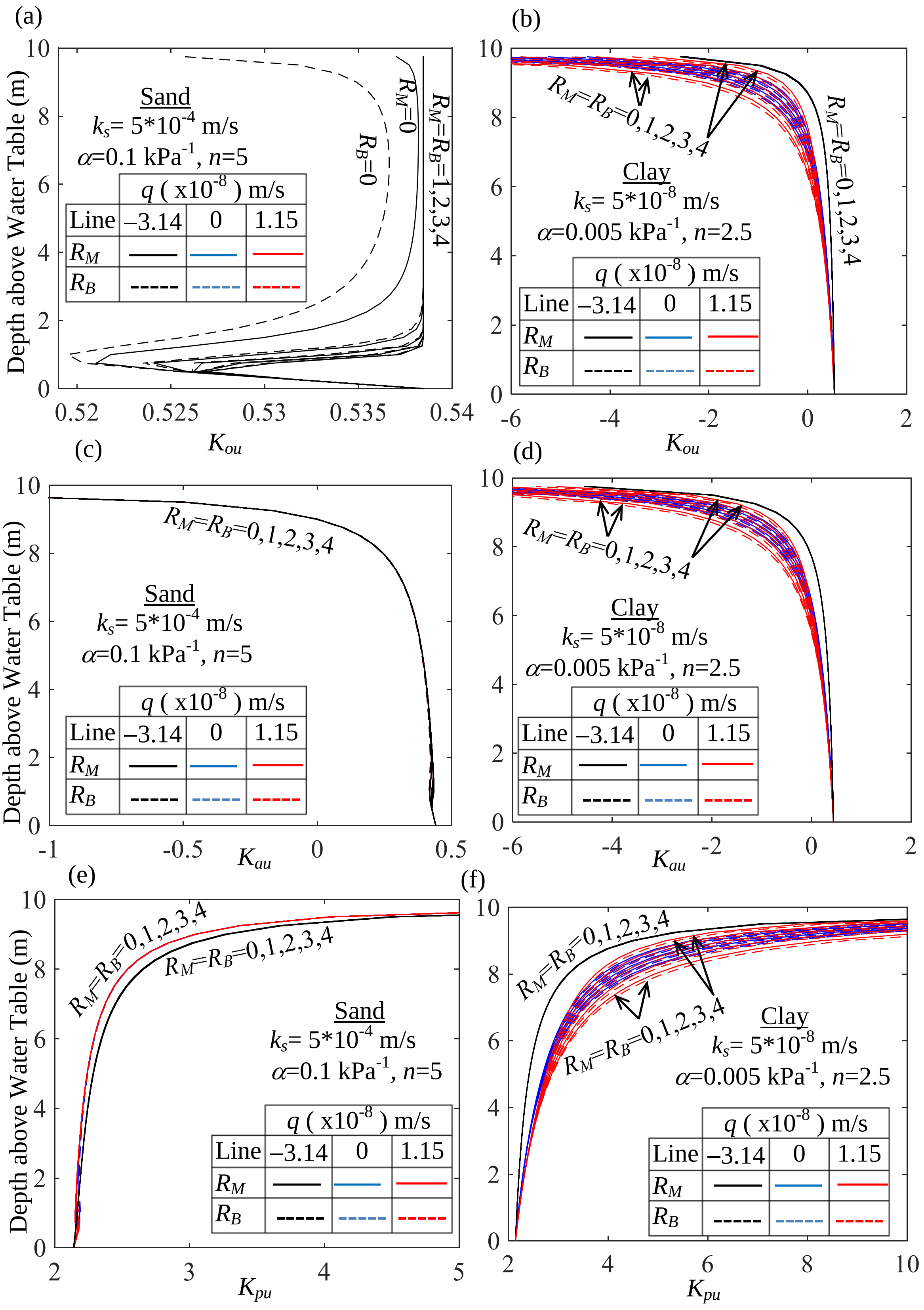

Fig. 8.3 The variation of K_{ou}, K_{au} and K_{pu} in the vadose zone for (a, c, e) sands, and (b, d, f) clays.

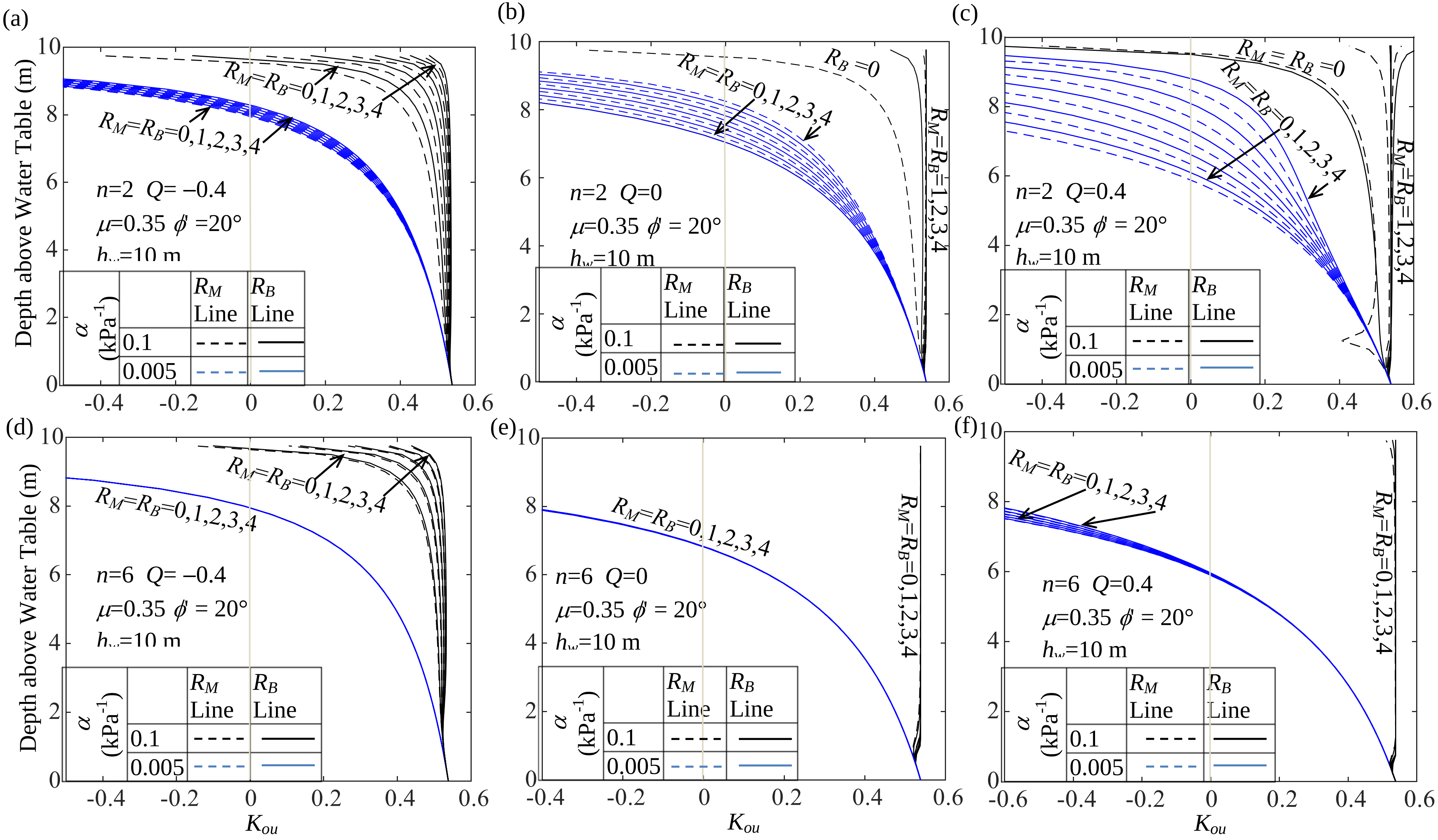

Fig. 8.4 The variation of K_{ou} above the water table for two α's with various m's and corresponding to (a) n=2, Q= −0.4; (b) n=2, Q= 0; (c) n=2, Q= 0.4; (d) n=6, Q= −0.4; (e) n=6, Q= 0; (f) n=6, Q= 0.4.

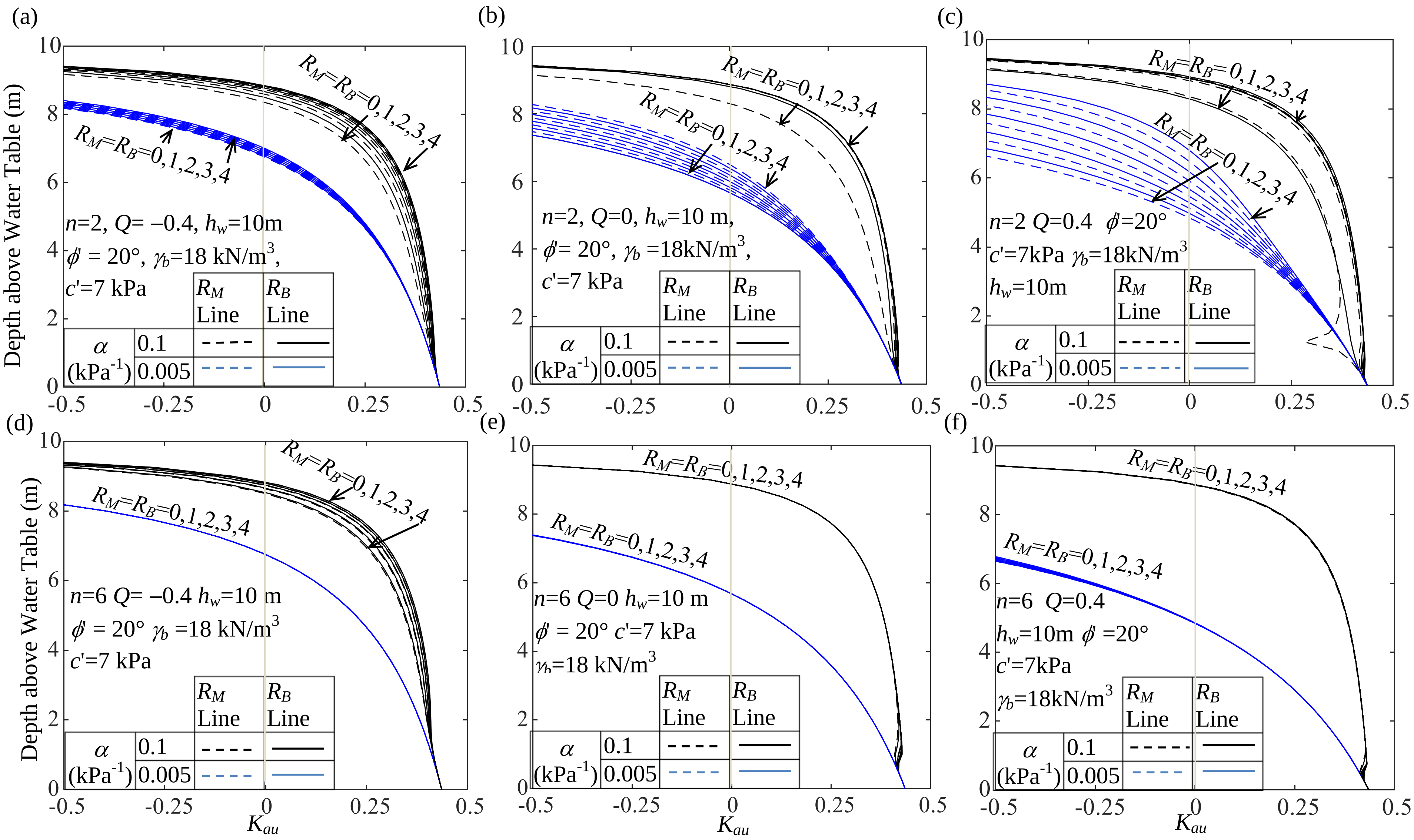

Fig. 8.5 The variation of K_{au} above the water table for two α's with various m's and corresponding to (a) $n=2$, $Q=-0.4$; (b) $n=2$, $Q=0$; (c) $n=2$, $Q=0.4$; (d) $n=6$, $Q=-0.4$; (e) $n=6$, $Q=0$; (f) $n=6$, $Q=0.4$.

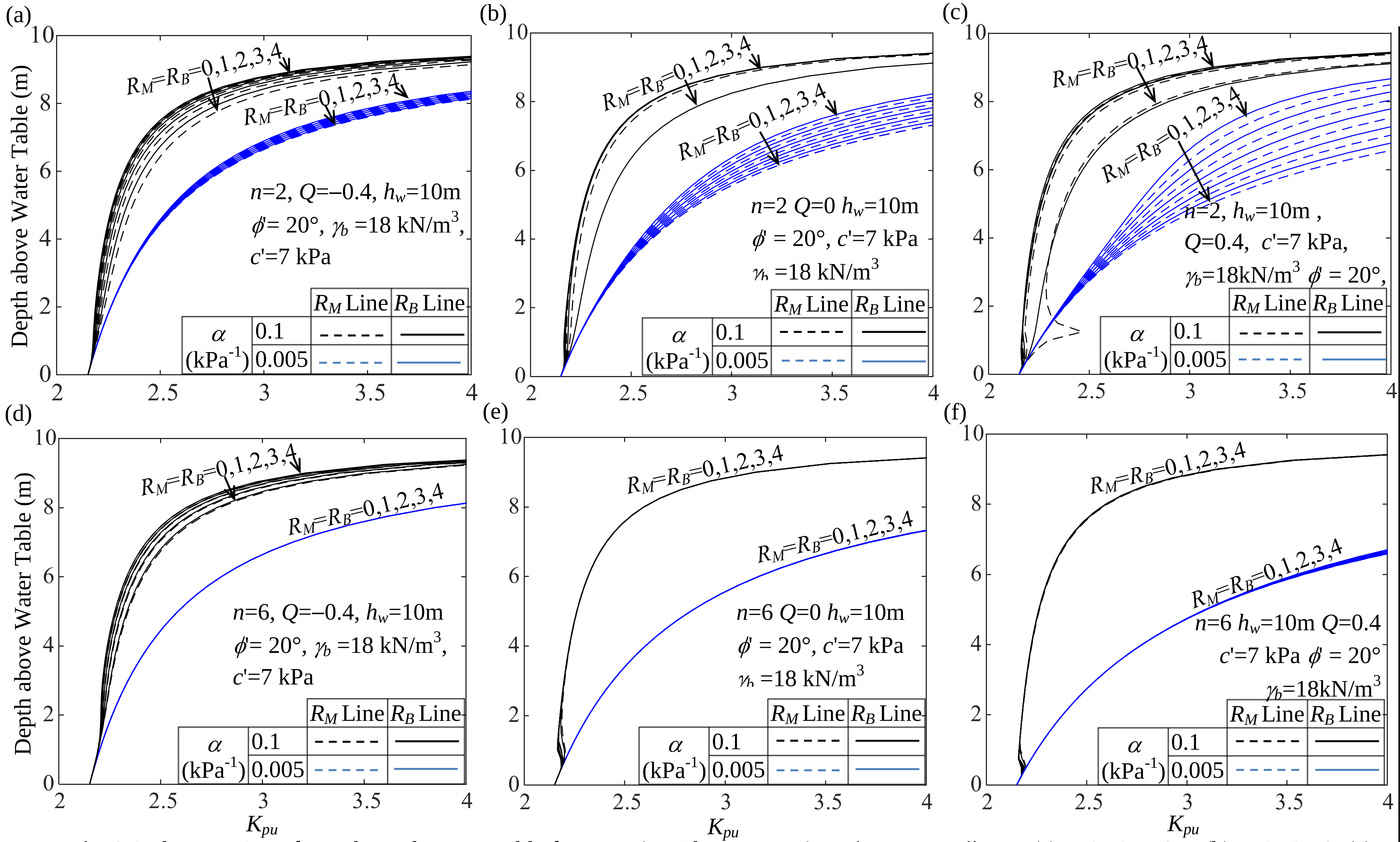

Fig. 8.6 The variation of K_{pu} above the water table for two α's with various m's and corresponding to (a) n=2, Q= –0.4; (b) n=2, Q= 0; (c) n=2, Q= 0.4; (d) n=6, Q= –0.4; (e) n=6, Q= 0; (f) n=6, Q= 0.4.

(a) Upto a certain height above the water table, the EP profiles are unaffected by R_M and R_B. This is the zone that seems entirely immune to the effect of *m* parameter. This can be attributed due to the extent of capillary saturation regime which is higher for α =0.005 kPa^{-1} than α =0.1 kPa^{-1}. The thickness of this zone is highest for the infiltration followed by the no-flow condition and becomes least while the soil dries up.

(b) During the wetting of soils, the *m* parameter does not influence the earth pressure profiles much. The impact of chosen *m* value becomes visible for the no-flow condition and it becomes pretty significant during the drying of soils.

(c) The argument of choosing appropriate *m* becomes important when the soil is well-graded. Regardless of the *m*-value, the earth pressure profiles remain unaffected for uniformly graded soil.

(d) Corresponding to Q=0.4 and n=2, the R_M and R_B lines become relatively more distinct for α = 0.005 kPa^{-1} in comparison to α = 0.1 kPa^{-1}.

8.2.4.1.3 *Crack Depth profiles versus α*

Figs. 8.7 and 8.8 depict the variations of crack depth with respect to the α-parameter (termed here as *CD−α profiles*) corresponding to the rest and active failure states, respectively. The graphs are plotted for three different values of *n* (= 2.5, 4.5, and 8.5) and two *Q*'s, namely, 0 and −0.4. Fig. 8.9 further represents the influence of frictional strength on the CD profiles; the curves are drawn for ϕ=20°, 30°, and 40° soil. The figures provide the following impressions:

(a) Upto a certain α, referred here as divergent α (α_{div}), the crack depth remains the same and unaffected by R_M and R_B; beyond α_{div}, the *CD−α profiles* decrease at different rates on the basis of *m* value. The magnitude of α_{div} is relatively higher for (i) stronger soils, (ii) larger *n*, and (iii) wetting phenomenon.

(b) The decrementrate of the *CD−α profiles*is steepest for higher values of R_M and R_B and the slope of the *CD−α profiles* decreases with the subsequent reduction in R_M and R_B. Therefore, for a certain flow condition, irrespective of the soil type, the lower the *m*, the larger is the crack depth.

(c) The *CD−α profiles* become steeper for higher *n* and no-flow condition than its infiltration counterpart. Further, the friction strength of the soil impacts the crack development markedly. Stronger soil results in larger crack depth and a sharp decline in the *CD−α profiles*.

(d) For weaker soils with smaller *m*'s, the *CD−α profiles* tend to have a flatter curve.

(e) The differences in the *CD−α profiles* are significantly visible when the R_M and R_B are taken to be zero. As the values of R_M and R_B increase, the deviations between the *CD−α profiles* diminish. The variation between the R_M and R_B lines becomes negligible for poorly graded soil.

(f) The suction stress-induced crack depth, as illustrated in Fig. 8.8c, ceases to develop for soil with relatively low AEV. At large α values, the curves merge and asymptote to a horizontal plateau, which precisely indicates the cohesion-induced crack depth (nonzero value for active state).

8.2.4.1.4 *Crack Depth profiles varying with Q*

Fig. 8.10 presents the variations of crack depth with respect to the Q parameter (termed here as *CD–Q profiles*) for various combinations of α and *n* corresponding to lateral-restraint deformation as well as horizontal stress relaxation. The following observations are recorded:

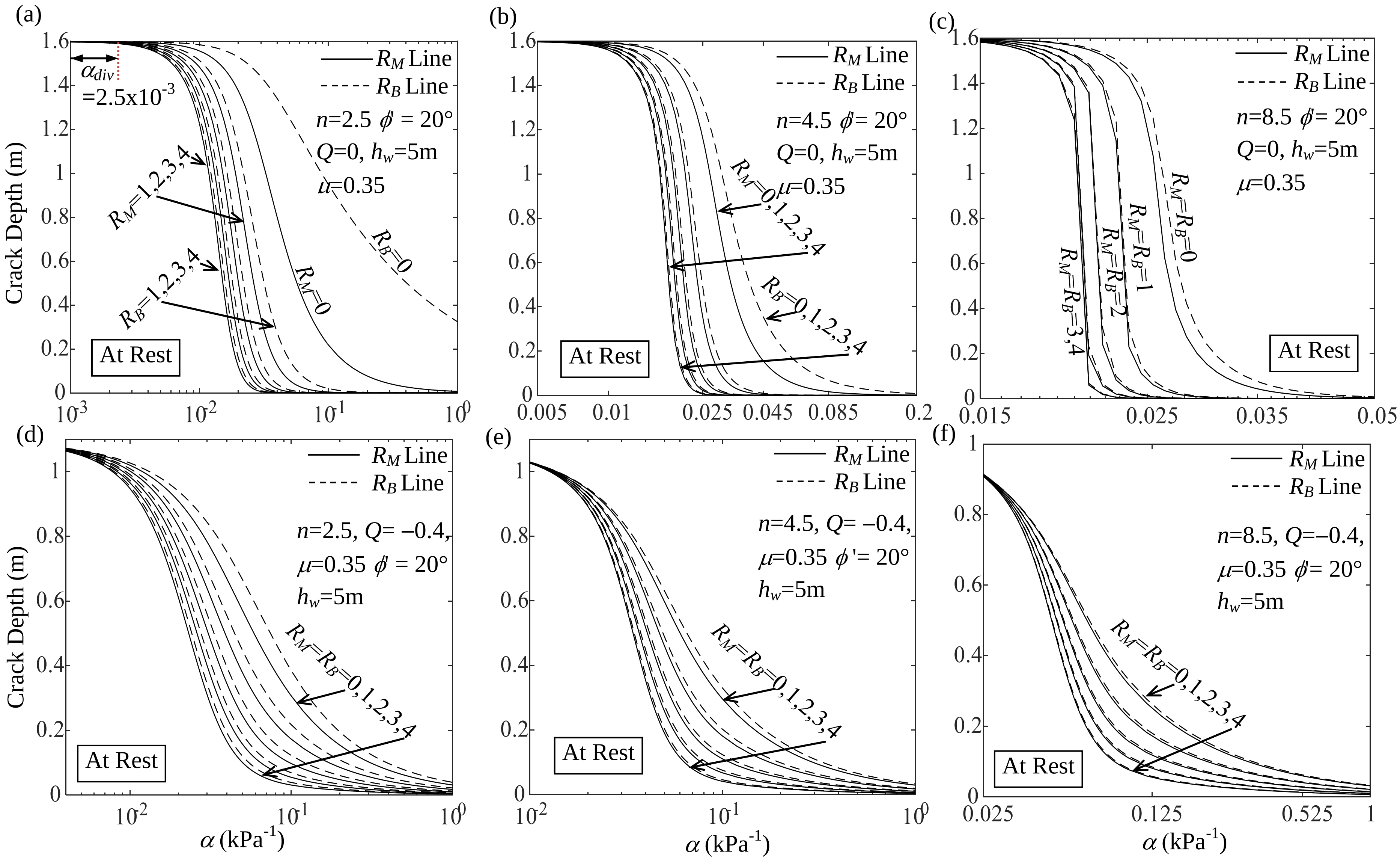

Fig. 8.7 The variation of crack depth with α for various *m* subjected to rest condition and corresponding to (a) *n*=2.5, *Q*= 0; (b) *n*=4.5, *Q*= 0; (c) *n*=8.5, *Q*= 0; (d) *n*=2.5, *Q*= –0.4; (e) *n*=4.5, *Q*= –0.4; (f) *n*=8.5, *Q*= –0.4.

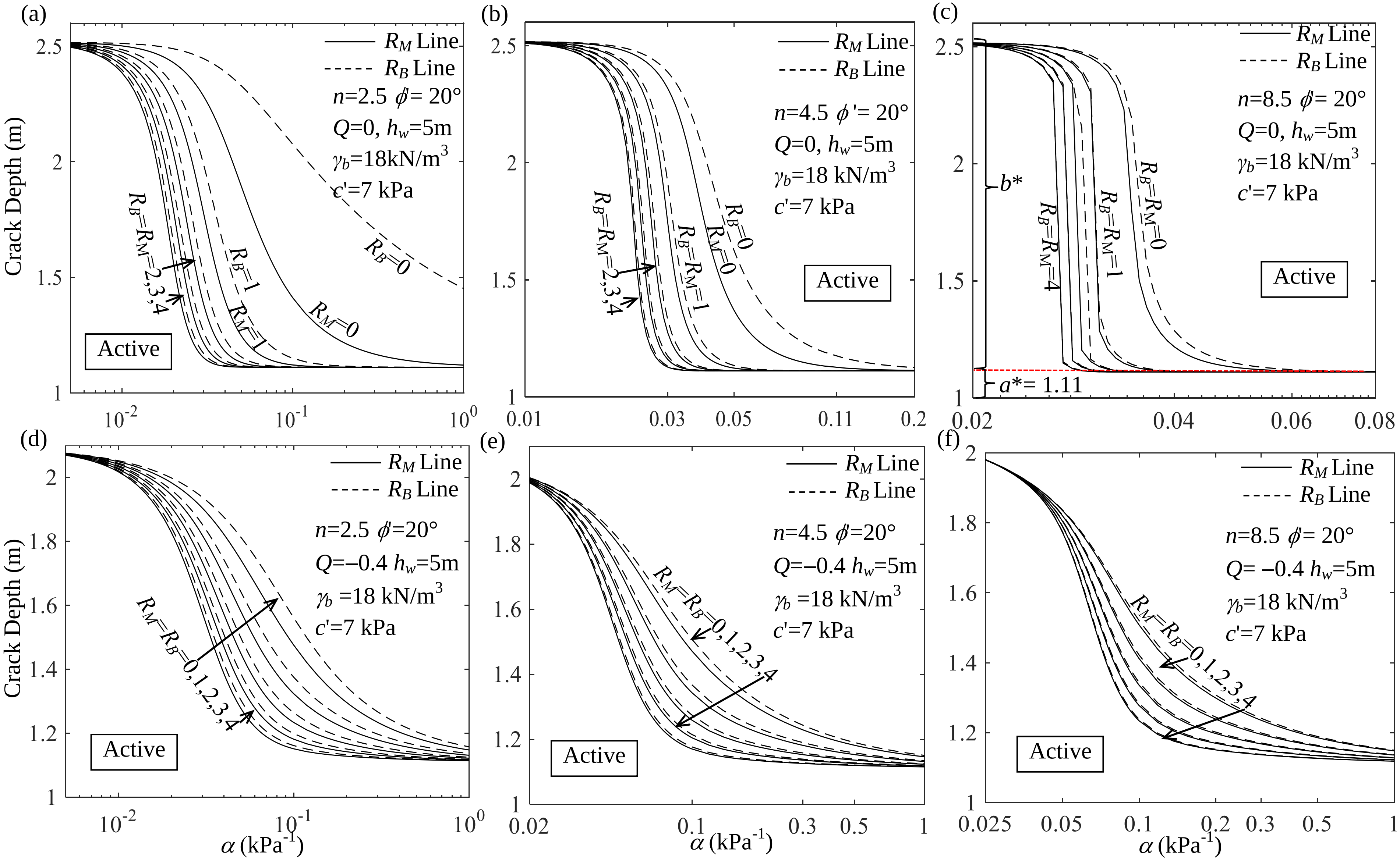

Fig. 8.8 The variation of crack depth with α for various m subjected to active condition and corresponding to (a) n=2.5, Q= 0; (b) n=4.5, Q= 0; (c) n=8.5, Q= 0; (d) n=2.5, Q= –0.4; (e) n=4.5, Q= –0.4; (f) n=8.5, Q= –0.4.

***Note**: a-Cohesive TCD; b-Suction TCD

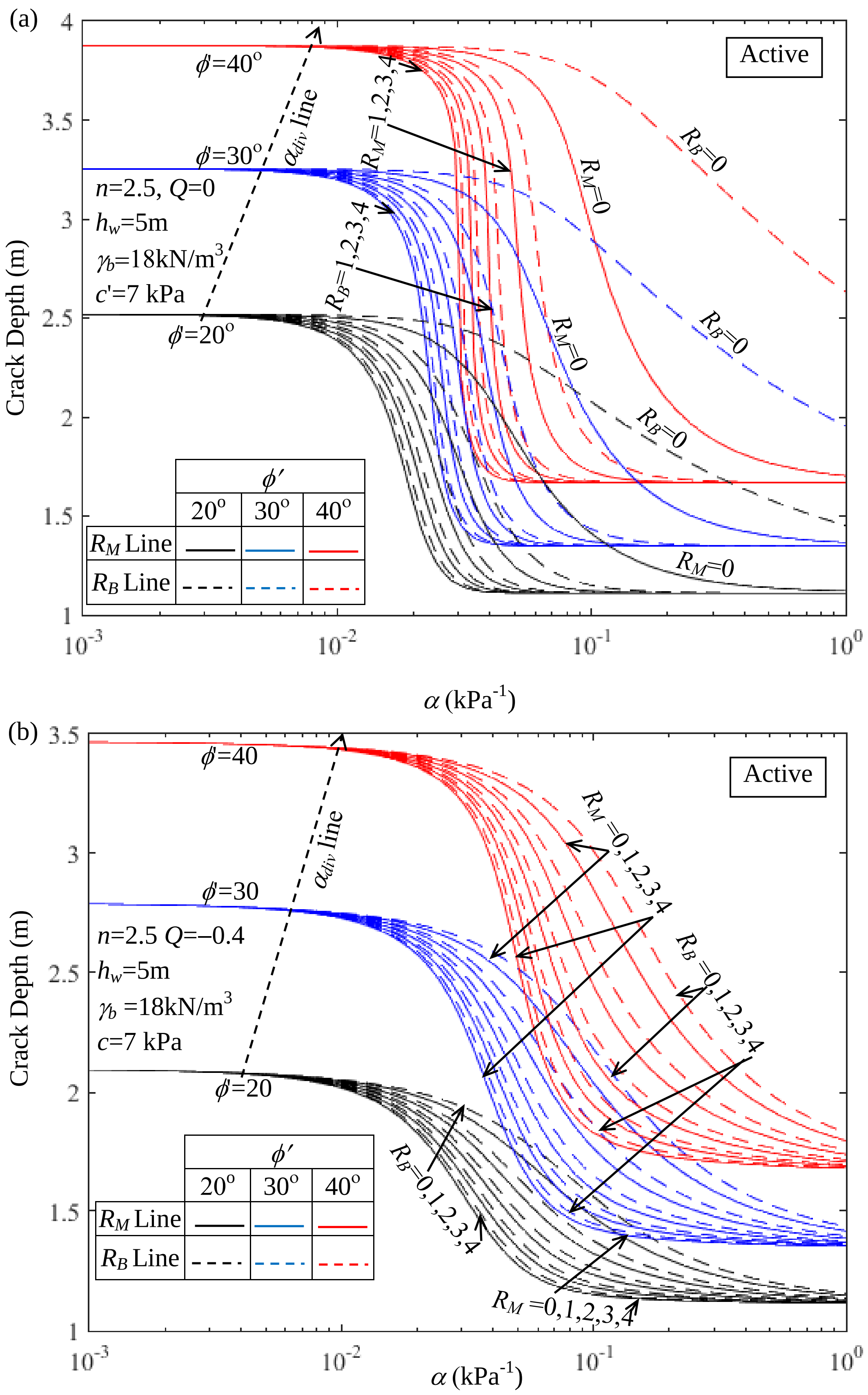

Fig. 8.9 The variation of crack depth with α for different ϕ' and m subjected to active condition and corresponding to (a) Q= 0; (b) Q= – 0.4.

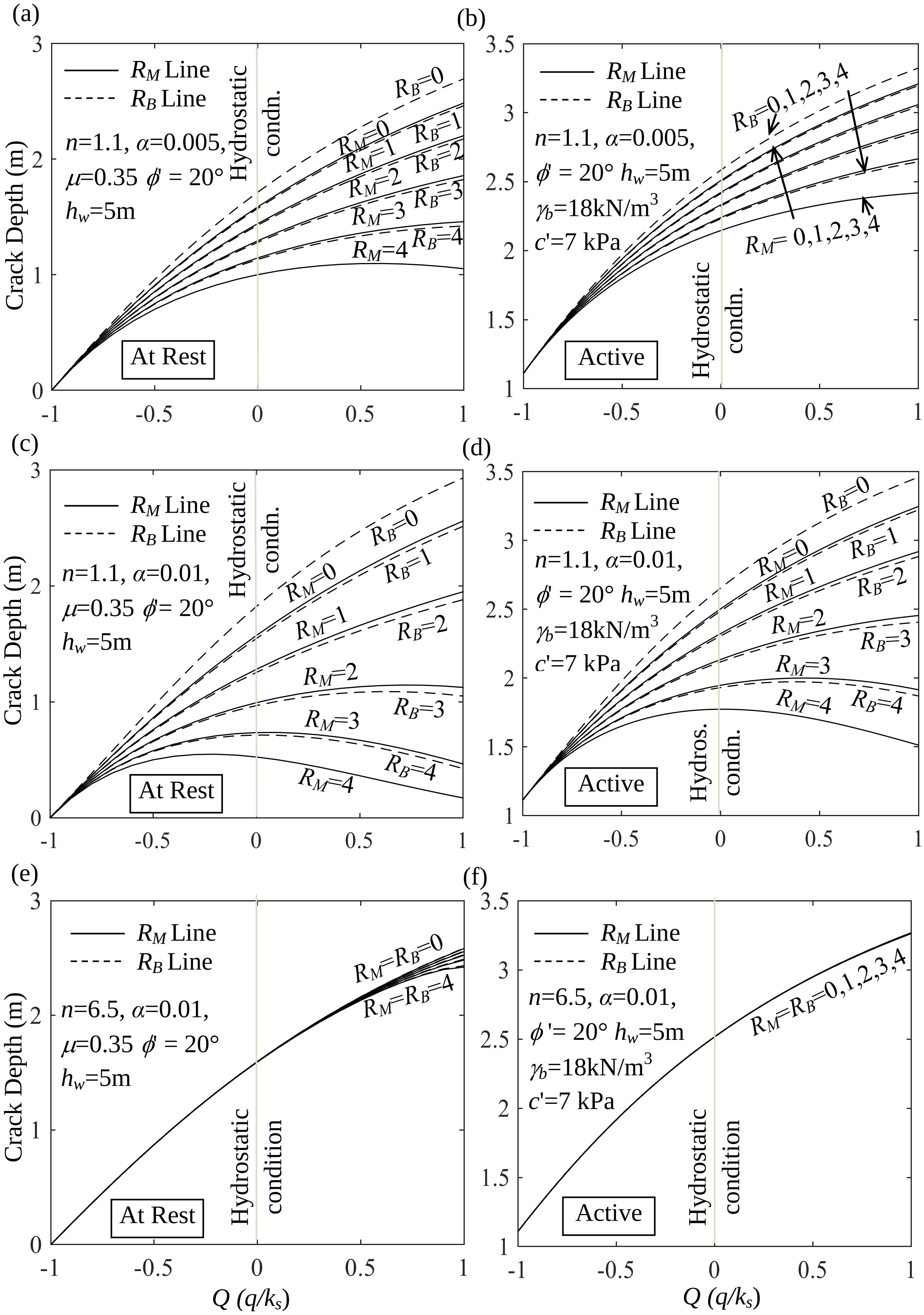

Fig. 8.10 The variation of crack depth with Q for various m subjected to rest condition ((a) n=1.1, $\alpha = 0.005$, (c) n=1.1, $\alpha = 0.01$, (e) n=6.5, $\alpha = 0.01$) and active condition ((b) n=1.1, $\alpha = 0.005$, (d) n=1.1, $\alpha = 0.01$, (f) n=6.5, $\alpha = 0.01$).

(a) The *CD–Q profiles* increase continuously but at a decreasing rate; at certain Q values (+ve) the curves attain a horizontal plateau. The attainment of constant TCD is faster for well-graded soils with high m.

(b) For a high rate of infiltration, m parameter hardly influences the *CD–Q profiles*. The dispersion of the *CD–Q profiles,* which evolve from various m, widen as the flow alters from low percolation to hydrostatic to evaporative condition.

(c) Further, this dispersion of the *CD–Q profiles* in the evaporative zone expands for (i) rest state, (ii) higher α, and (iii) low n. Corresponding to Q=1, and n=1.1, while m varies from 0.091 to 4.091, the difference in the evaluated TCD is (a) 57.64% and 93.31% for the rest state and (b) 24.64% and 53.46% for the active state pertaining to α equals 0.005 to 0.01 kPa^{-1}, respectively.

(d) For n=6.5, even for the rest state and maximum considered drying stage the deviation in the *CD–Q profiles* is insignificant.

8.2.4.1.5 *Total active earth pressure profiles - Active State*

Fig. 8.11 depicts the variation of AEP profiles in the vadose zone corresponding to various R_M and R_B and different values of α (=0.01 and 0.005 kPa^{-1}) and n (=2.5 and 6.5) parameters. The profiles are drawn for three specific flow rates, namely, Q= –0.8, 0, and 0.8. During the hydrostatic condition, the m parameterinfluences the AEP profiles moderately if the soil is of well-graded silty types (α = 0.01 and n = 2.5). On the other hand, the curves representing the infiltration case are not at all influenced by the R_M and R_B parameters. But the curves emanating from the evaporative condition are highly controlled by the m parameter. During the drying up of the unsaturated zone, the fluid flow direction and the vG-SWCC parameters combinedlyaffect the (a) curvature of the AEP profiles, (b) degree of divergence, and (c) spatial position at which the deviation begins to be visible in the R_M and R_B lines. The observations corresponding to the evaporation are summarized as follows:

(a) Up to a certain level above the water table, referred here as z_0 and shown in Fig. 8.11a, the R_M and R_B lines collapse onto a single curve and within z_0 the drying phenomenon always generates a higher amount of tensile AEP than the wetting phase. Above that level, the R_M lines predict lesser tensile stress than the R_B one. The z_0 remains at an elevated position (from the water table) for higher n and lower α. Moreover, with the increase in m, the tensile stress decreases at the top surface.

(b) The effects of R_M and R_B become significantly prominent for lower n and higher α values. As the pore size becomes uniform, the tensile AEP decreases, and the deviation range corresponding to the least and the maximum m narrows down. For the same distribution of pores, the difference between the AEP profiles gets widened for $\alpha = 0.01$ kPa^{-1} compared to $\alpha = 0.005$ kPa^{-1}.

(c) For higher m's, the evaporative profiles for α=0.01 kPa^{-1} touch the ground surface even at a lesser magnitude of tensile AEP than the no-flow and the infiltrative profiles.

(d) The AEP profiles' curvature regarding the evaporative condition reduces significantly for high AEV soils. Hence, the evaporative profiles result in the largest tensile AEP at the ground surface, even for the maximum chosen value of m.

8.2.4.1.6 *Component of Earth pressure Due to suction stress- Passive state*

The PEP components due to the suction stress (σ_{Suc}^{PEP}), as shown in Fig. 8.1c, are depicted in Fig. 8.12 on the basis of various R_M and R_B values. The analyses are performed corresponding to three α's (=0.1, 0.01, and 0.001), two n's (=2.5, and 4),

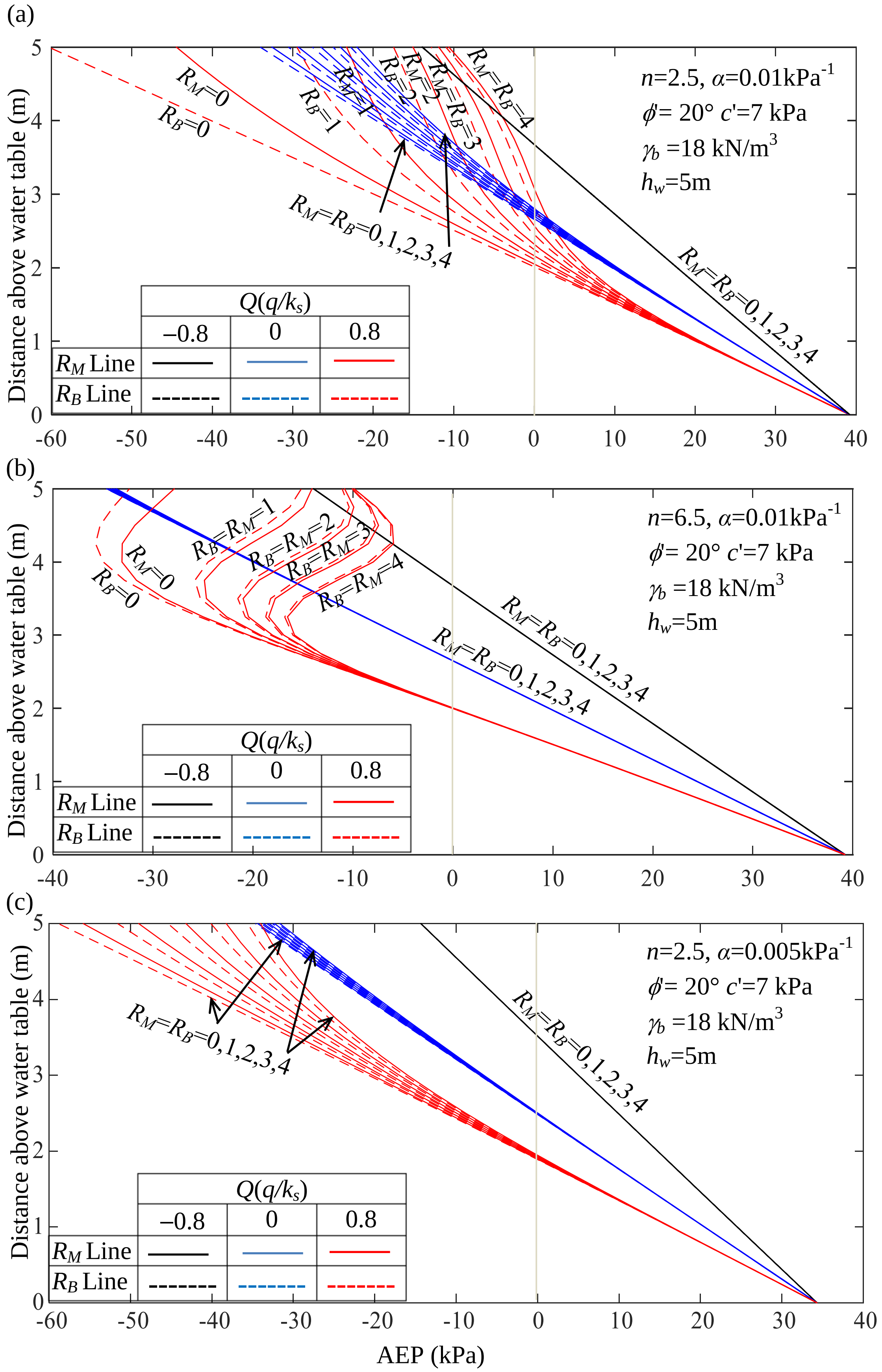

Fig. 8.11 The variation of AEP above the water table for various *m* subjected to different *Q* and corresponding to (a) *n*=2.5, $\alpha = 0.01$; (b) *n*=6.5, $\alpha = 0.01$; (c) *n*=2.5, $\alpha = 0.005$.

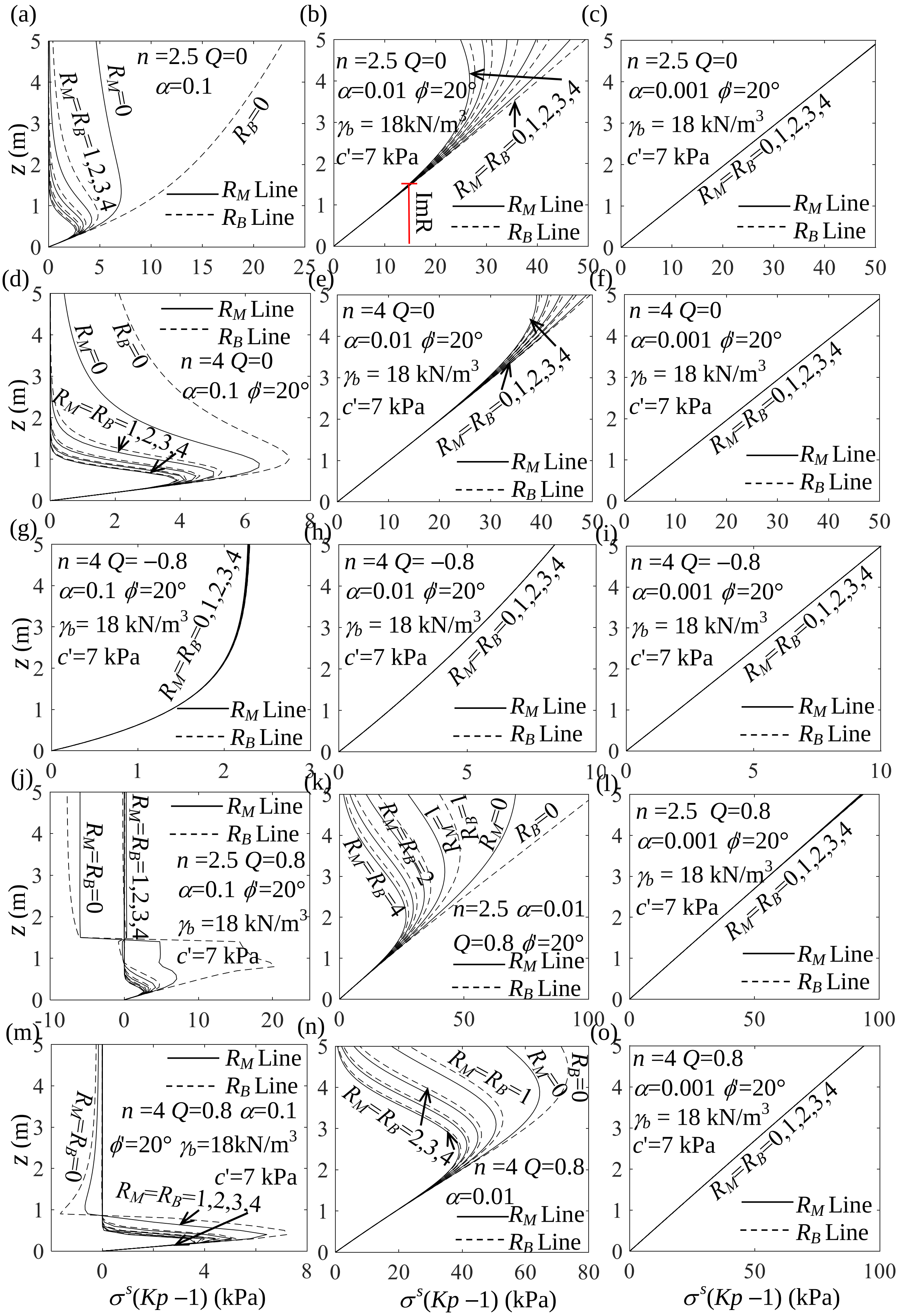

Fig. 8.12 The variation of σ^s induced PEP component above the W.T.(z) for various *m* subjected to passive condition and corresponding to (a-f) *Q*=0, (g-i) *Q*=–0.8, (j-o) *Q*=0.8; (a-c, j-l) *n*= 2.5, (d-f, g-i, m-o) *n*= 4; and (a, d, g, j, m) α=0.1, (b, e, h, k, n) α=0.01, (c, f, i, l, o) α=0.001.

and three Q's (–0.8, 0.0, and 0.8). From the drawn graphs, the following few points can be made:

(a) Apart from a few specific soils (i.e., α=0.1 soil with R_M and R_B =0) in the evaporative condition, the σ_{Suc}^{PEP} remains non-negative throughout the vadose zone for all the cases. It indicates the increment of the PEP above the water table in contrast to the saturated soils. Moreover, for lower α, the variation of PEP becomes highly non-linear. The nonlinearity of the PEP profile decreases for high AEV soils.

(b) There is a certain region above the water table where the σ_{Suc}^{PEP} does not depend upon the m parameter. The extent of this insensitive m-region (shown as '*ImR*' in Fig. 8.12b) grows in size with the increase in n and decrease in α. For instance, considering n =2.5 and Q=0, the magnitude of *ImR* turns out to be 0.2, 1.8, and 5 corresponding to α=0.1, 0.01, and 0.001, respectively. For soils with high AEV, the impact of m parameter on the PEP profiles is maximum at the ground surface.

(c) Corresponding to low AEV soils (say, AEV<10kPa), the σ_{Suc}^{PEP} increases linearly up to a small depth above the water table and after that, it starts to decrease and eventually attains a zero value. The decrement rate is excessively high for larger m and n values. Thus, the nature of the curve shows an existence of pronounced peak PEP profiles. With the increase in m, this peak point occurs at a lower depth with lesser values.

(d) The magnitude of σ_{Suc}^{PEP} decreases significantly with the increase in α value, especially for the evaporative condition. Corresponding to a specific value of α, higher the n higher is the value of σ_{Suc}^{PEP}; this phenomenon is more appreciable for low AEV soils.

(e) It is also noticed that the PEP is maximum for drying and minimum for wetting.

(f) The impact of *m* parameter on the σ_{Suc}^{PEP} is pronounced for evaporation, followed by the hydrostatic condition. For the chosen infiltration rate, it is observed that irrespective of α, all the R_M and R_B lines are identical.

(g) With the increase in *m* values, the suction stress-induced PEP component adjacent to the ground surface decreases to a noticeable extent for α=0.01 kPa^{-1} and non-negative flow ratios. R_M lines encompass a relatively smaller amount of stress area than its R_B counterpart.

(h) The deviations between the various R_M and R_B lines get narrower with the increase in *n* and decrease in α. In other words, the impact of *m* becomes significant for lower *n* and higher α.

(i) The impact of the *m* parameter is significantly palpable when *m* changes in the lower ranges. For instance, increasing the R_M (or R_B) value from 0 to 1 influences the PEP profiles remarkably; nevertheless, the deviation of the PEP profiles almost ceases to exist for any further increment of R_M (or R_B) beyond 3.

8.2.4.2 Effect of Gardener's two parameter HCF model (1958)

Fig. 8.13 shows the variations of EP profiles above the water table by considering Gardner's OPM and TPM. The figures are produced for rest, active and passive state conditions corresponding to two different values of α, namely, 0.005 and 0.01 kPa^{-1}. Five values of ξ, namely, 1, 2, 3, 4, and 5 are used in the analysis. The TPM solutions were attainable for the entire spectrum of *Q*, when ξ was taken to be either 1 or 2. For $\xi \geq 3$, the suction stresses are deducible only for high infiltration rates. Other flow rates result in undefined numeric values. The reason may be attributed to the nature of the suction stress relationships with the spatial coordinates. For any arbitrary depth, suction stress and subsequently the EP's can explicitly be evaluated (Appendix C) if the exponent parameter in TPM models (i.e. ξ) is taken to be either 1 or 2. The closed-form expression of suction stress with respect to z cannot be obtained for ξ =3, 4, 5, and so on. The implicit expressions provided in Eqs. C.4-C.6 are solved by using Newton-Raphson as well as the Gauss-Newton iteration technique. It is to be noted that for the purpose of numerical simplicity and flexibility, ξ is forcibly taken as integer values, but ξ can also be a fractional value.

From Fig. 8.13, it can be vividly observed that TPM models corresponding to ξ= 1 and 2 coincide with each other. For higher values of ξ, till ξ = 4, TPM model predicts less EP than the OPM. Hence, corresponding to rest and active states, larger TCDs are estimated while $\xi \leq 4$. But surprisingly, the curve corresponding to ξ = 5 remains at the top for all the three earth pressure states. Therefore, no definitive statement can be made about the trends of the curve with an increase in ξ. The closeness of the OPM and TPM with ξ = 1 or 2 becomes prominent for high AEV soils. The deviations in the curve seem to be prominent in the compressive zone rather than the tensile section. It is to be noted from Fig. 8.2b that change in ξ not only influence the desaturation rate but it also lays its impact on the matric suction value at which desaturation commences.

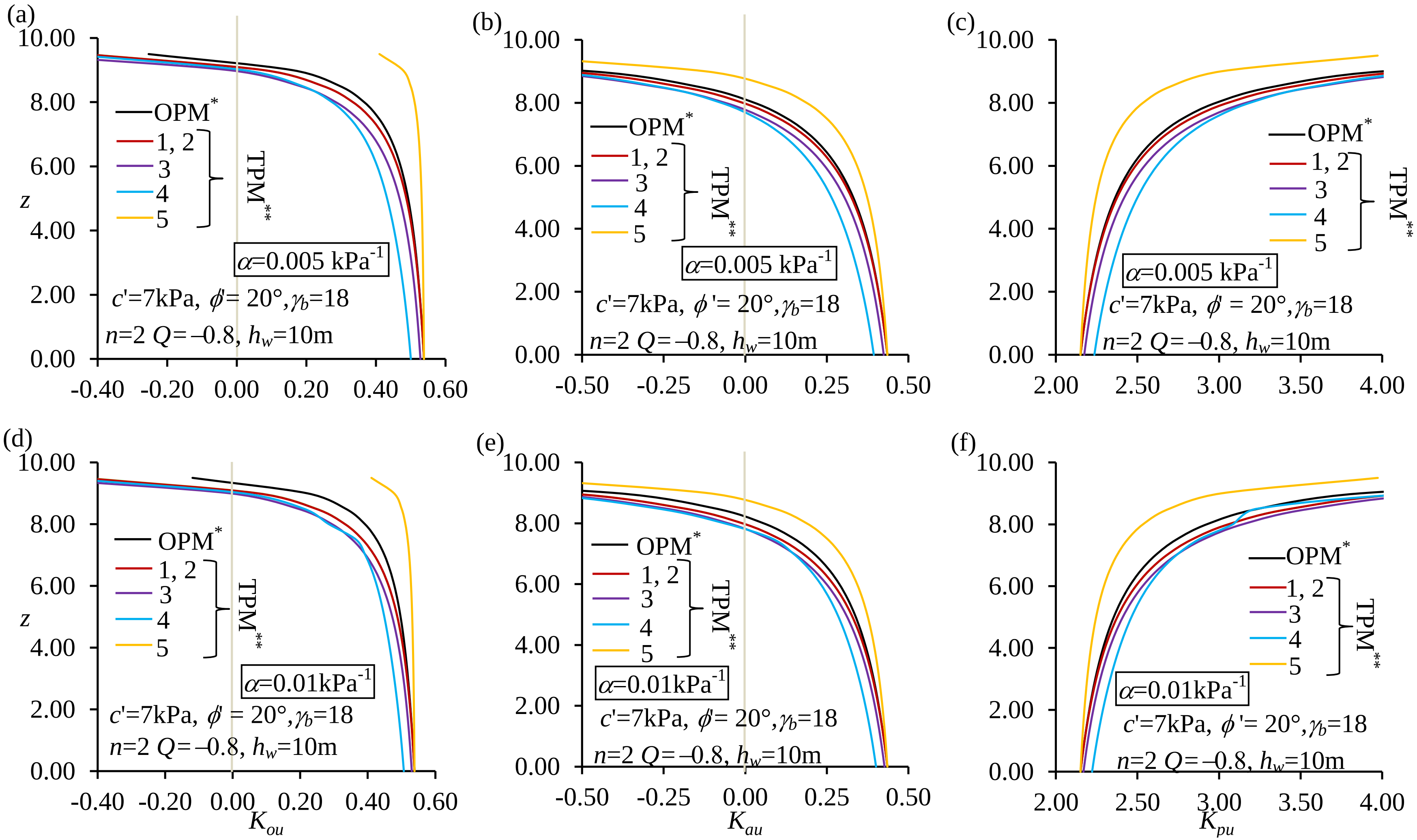

Note:*OPM= Gardener's one parameter model, **TPM= Gardener's two parameter model

Fig. 8.13 The variation of K_{ou}, K_{au} and K_{pu} above the W.T.(z) for rest- (a, d), active- (b, e) and passive – (c, f) condition respectively with a-c $\alpha = 0.01$ and d-f $\alpha = 0.005$ subjected to OPM and TPM.

8.3 MODIFICATION AND APPLICATION OF COULOMB’S METHOD FOR ADDRESSING INCLINED RETAINING WALL SUPPORTING UNSATURATED BACKFILL WITH INCLINED SURFACE

8.3.1 Problem statement

An inclined wall (AO) of height, H, and inclination angle, β, retains a homogeneous, isotropic and cohesive-frictional soil which is under partially saturation state. The ground surface of the backfill is inclined at an angle i. The schematic diagram of the considered problem is shown in Fig. 8.14. The roughness condition of the soil-wall interface is realized by the interface angle, δ. The backfill is subjected to certain seismic activities. The vertical distance between the ground water table (GWT) and the top point of the wall is h_w. The soil above and below the GWT is under partially saturated and fully saturated conditions, respectively. The unsaturated properties of the vadose zone are incorporated in the formulations with the adequate induction of the SSCC, as demonstrated in Section 6.2.1. The pseudo-static method is used for factoring the seismic effect into the problem. The prime objective of the study is to comprehend the combined impact of geometric parameters, soil strength parameters, SWCC parameters, surface flow ratio, and seismic loading on active earth pressure by employing modified Coulomb’s earth pressure theory.

8.3.2 Formulations

Fig. 8.14 depicts the geometry of the considered failure wedge, AOB. The failure surface OB is inclined at an angle of ζ with the horizontal surface. The internal and external forces acting on the OAB wedge are displayed in the figure. The concerned forces are:

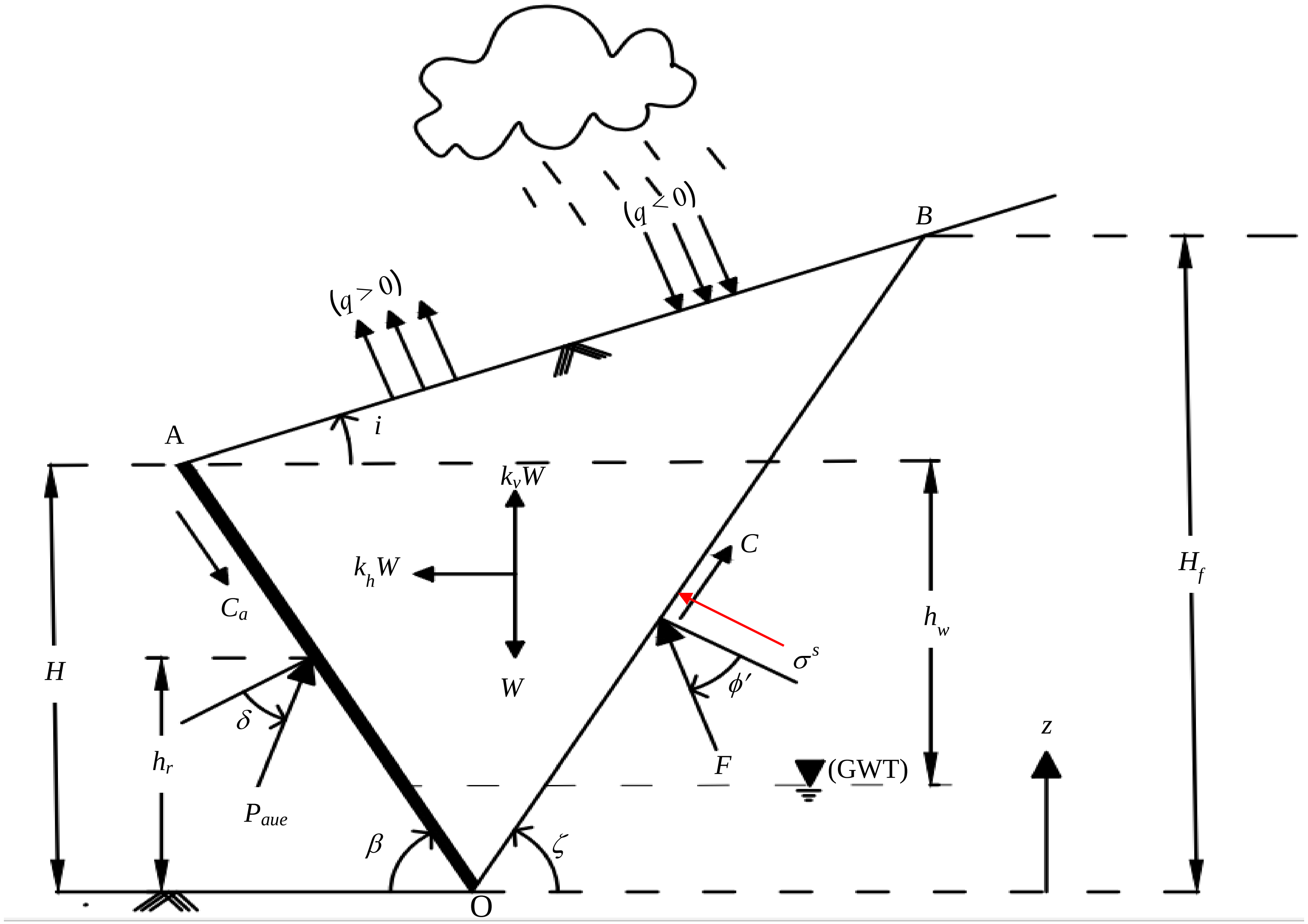

Fig. 8.14 Schematic representation of an inclined retaining wall supporting unsaturated sloped backfills subjected to seismic forces.

(a) Self-weight of the wedge: W

(b) Pseudo-static horizontal (k_hW) and vertical (k_vW) inertial forces (Notably, the force due to k_v acts in the vertically upward direction)

(c) Forces acting on the backfill-wall interface OA:

  (i) The effective adhesive force (C_a)

  (ii) The total active thrust due to seismic forces for unsaturated soil (P_{aue})

(d) Forces acting on the failure surface OB:

  (i) Resultant force (F)

  (ii) Total cohesive force: $C = \dfrac{c'H_f}{\sin\zeta} + \dfrac{A}{\sin\zeta}$; where $A = \displaystyle\int_{z=0}^{z=H_f} \sigma^s \tan\phi' dz$ (8.9)

The expression of σ^s is obtained from Eq. (6.11). Notably, computing the analytical expression of A becomes a very challenging task. Therefore, the domain above the GWT is discretized with finite number of small elements and the value of A is numerically evaluated by using the trapezoidal rule.

In this section, the equations are formulated to evaluate the following two terms:

8.3.2.1 Determination of seismic active earth pressure coefficient on unsaturated soil (K_{aue})

The following steps are involved:

Step 1: Resolving the forces along horizontal and vertical direction and implementing the force equilibrium equation:

$$P_{aue}\sin(\beta-\delta) - F\sin(\zeta-\phi') - k_hW + C\cos\zeta - C_a\cos\beta = 0 \quad (8.10)$$

$$W - k_vW - F\cos(\zeta-\phi') - C\sin\zeta - P_{aue}\cos(\beta-\delta) - C_a\sin\beta = 0 \quad (8.11)$$

Step 2: Solving Eqs. (8.10) and (8.11) the total active pressure can be obtained as follows:

$$W(1-k_v)-\left[P_{aue}\sin(\beta-\delta)-k_hW+C\cos\zeta-C_a\cos\beta\right]\cot(\zeta-\phi')-C\sin\zeta \\ -P_{aue}\cos(\beta-\delta)-C_a\sin\beta=0 \tag{8.12a}$$

$$\Rightarrow P_{aue}=\frac{W(1-k_v)-(C\cos\zeta-k_hW-C_a\cos\beta)\cot(\zeta-\phi')-C\sin\zeta-C_a\sin\beta}{\dfrac{\sin(\beta-\delta)}{\tan(\zeta-\phi')}+\cos(\beta-\delta)} \tag{8.12b}$$

$$=\left[\frac{\begin{matrix}W\left\{(1-k_v)+k_h\cot(\zeta-\varphi')\right\}-C\left\{\sin\zeta+\cos\zeta\cot(\zeta-\varphi')\right\}\\ -C_a\left\{\sin\beta-\cos\beta\cot(\zeta-\varphi')\right\}\end{matrix}}{\sin(\zeta-\varphi'+\beta-\delta)}\right]\times\sin(\zeta-\varphi') \tag{8.12c}$$

Step 3: Computing the weight of the failure wedge AOB:

$$W=\frac{1}{2}\mathrm{AO}\times\mathrm{OB}\times\sin(\zeta+\beta) \qquad \text{; where, } \mathrm{AO}=\frac{H}{\sin\beta} \tag{8.13}$$

The expression of OB can be obtained from the sine rule:

$$\frac{\sin(\beta+i)}{\mathrm{OB}}=\frac{\sin(\zeta-i)}{\mathrm{OA}}\Rightarrow\mathrm{OB}=\frac{H}{\sin(\zeta-i)}\frac{\sin(\beta+i)}{\sin\beta} \tag{8.14}$$

Eventually, the expression of W becomes:

$$\Rightarrow W=\frac{1}{2}\gamma H^2\frac{\sin(\beta+i)\sin(\zeta+\beta)}{\sin^2\beta\sin(\zeta-i)}$$

Step 4: Maximizing P_{aue} with respect to ζ, The magnitude of ζ at which K_{aue} reaches its maximum value is termed here as the critical failure angle and designated as ζ_{cr},

Step 5: Obtaining coefficient of active earth pressure as: $K_{aue}=\dfrac{2\max(P_{aue})}{\gamma H^2}$ (8.15)

8.3.2.2 Deducing seismic active earth pressure distribution along depth (*p*$p_{aue}(z)$) on unsaturated soil

$$p_{aue}(z)=\left.\frac{\partial P_{aue}}{\partial z}\right|_{\zeta=\zeta_{cr}} \tag{8.16}$$

Solving Eq. (8.16), the expression of $p_{aue}(z)$ can be rewritten as:

$$p_{aue}(z) = \gamma(H - z)g_1 - (c' + \sigma^s \tan\phi')g_2 + C_a g_3 \tag{8.17}$$

Here,

$$g_1 = \frac{\sin(\beta + i)\sin(\zeta + \beta)[(1 - k_v) + k_h \cot(\zeta - \phi')]\sin(\zeta - \phi')}{\sin^2\beta \sin(\zeta - i)\sin(\zeta - \phi' + \beta - \delta)} \tag{8.18a}$$

$$g_2 = \frac{\cos\phi'}{\sin\zeta \sin(\zeta - \phi' + \beta - \delta)} \tag{8.18b}$$

$$g_3 = \frac{\tan\delta \cos(\beta + \zeta - \phi')}{\sin\beta \tan\phi' \sin(\zeta - \phi' + \beta - \delta)} \tag{8.18c}$$

8.3.3 Results and Discussions

This section conducts a comprehensive parametric analysis to evaluate the active earth pressure on a retained wall supporting an unsaturated inclined soil backfill subjected to pseudo-static forces. A detailed parametric study is conducted to understand the effect of wall (β) and backfill (i) geometries, backfill properties (ϕ', AEV, n), GWT location (h_w), wall-backfill interfaces (δ), flow ratios (Q) on the seismic active earth pressure coefficient for unsaturated soil (K_{aue}). Investigations are also carried out to understand the impact of a few parameters on the critical failure angle (ζ_{cr}), area of failure wedge (A_f). Except for one particular case, the effects of each of the parameters are observed and interpreted distinctly. Throughout the numerical simulations, the height of the wall and the unit weight of the backfill soil are taken to be 4m and 20 kN/m^3. During the examination of the material properties (saturated strength parameters and unsaturation parameters), the retaining wall is considered to be smooth (δ=0°) and vertical (β=90°), and the backfill soil is assumed to be horizontal (i=0°). Everywhere (except Section 8.3.3.4), the cohesive (c') and the frictional parameters (ϕ') are taken to be 4 kN/m^2 and 30°, respectively. Similarly, vG parameters are taken to be the same (α=0.005 kPa^{-1}, n=2) in all the simulations, except Section 8.3.3.6. The GWT is positioned at the toe of the retaining wall, barring the analysis done in presented in Section 8.3.3.7. The subsequent paragraphs elaborate on the salient observations from this study.

8.3.3.1 Impact of backfill inclination (i) on critical failure angle (ζ_{cr})

Fig. 8.15a shows the variation of critical failure angle ζ_{cr} with soil backfill angle, i, corresponding to different soil strength parameters (c', ϕ') and vG model parameters (α, n). For horizontal backfill (i.e., i=0°), ζ_{cr} becomes equal to $45^{o}+\phi'/2$. The air-entry value has a key role in determining the relationship between ζ_{cr} versus i. For low AEV, the ζ_{cr} reduces with i; whereas, for high values of AEV, $\zeta_{cr} - i$ profiles manifest increasing trends. The strength parameters also have a notable impact on the $\zeta_{cr} - i$ profiles. The higher the cohesion, the higher the predicted ζ_{cr}. With the increase in backfill inclination, the $\zeta_{cr} - i$ curves corresponding to different cohesive strength diverges; the higher the friction angle, the lower the divergence. The decreasing rate of $\zeta_{cr} - i$ profiles for low AEV soil gets suppressed with the (i) increase in ϕ', and (ii) decrease in desaturation rate.

8.3.3.2 Impact of backfill inclination (i) on the area of failure wedge (A_f)

An attempt has been made to check the effect of the soil's vG parameters and the strength parameters on the variation of the area encompassed by the failure wedge (A_f) at the optimal point. The variation of A_f with respect to i is demonstrated in Fig. 8.15b. The trend of the variation of A_f - i curve is completely reversed to what is being observed for $\zeta_{cr} - i$ profile. Irrespective of the frictional and the cohesive strength, the volume of the failure wedge is excessively high for the soils having relatively lower air-entry value. The figures also give an impression that for cohesionless soil, A_f grows

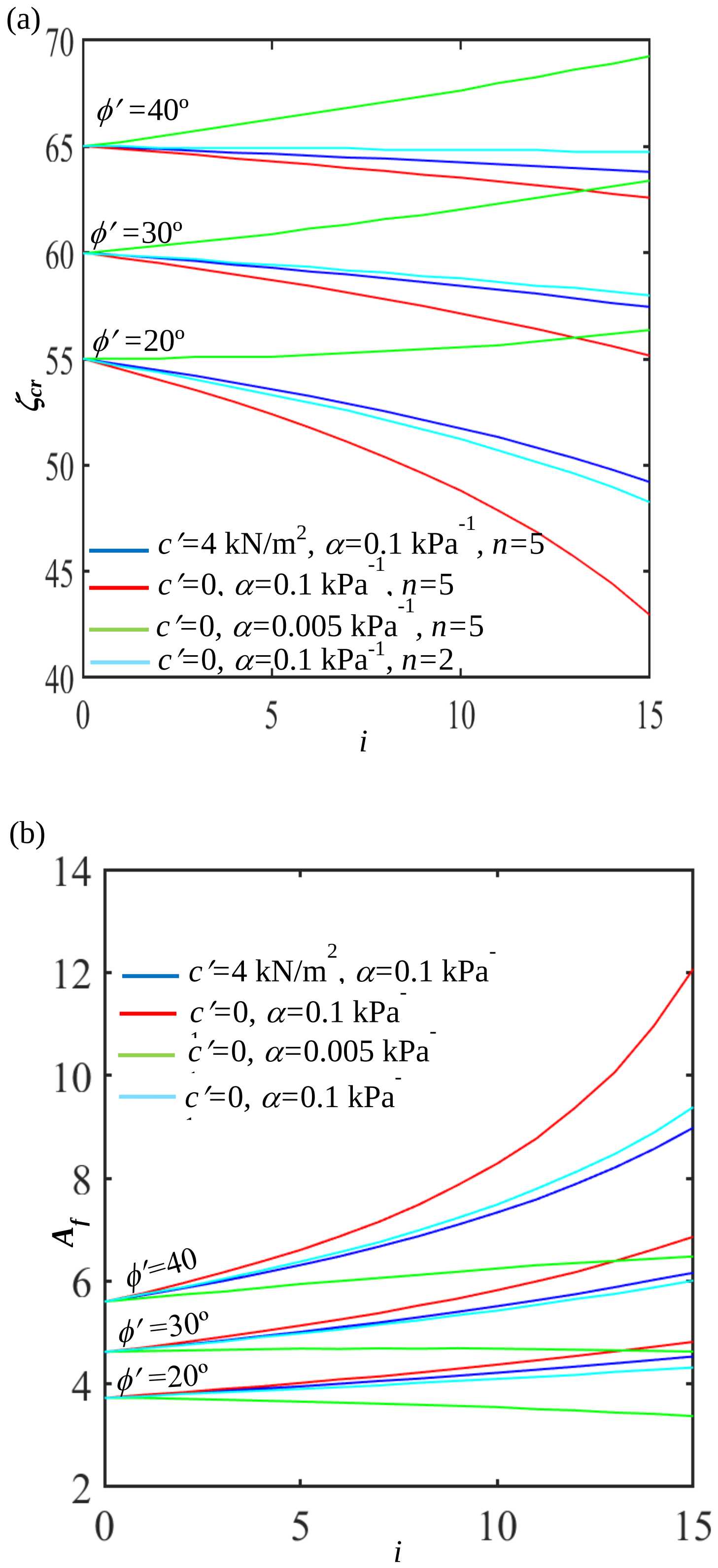

Fig. 8.15 The impact of backfill slope (i) on the (a) critical failure angle (ζ_{cr}) and (b) area of failure wedge (A_f).

more rapidly with the increase in backfill angle; however, the rate of this increment gets subdued if the frictional strength of the soil is less. An increase in cohesive strength and/or decrease in the pore spectrum number further results in reducing the magnitude of A_f.

8.3.3.3 Impact of backfill inclination and pseudo-static forces on K_{aue}

Fig. 8.16 illustrates the combined effect of backfill inclination (i) and horizontal seismic coefficient (k_h) on the computed seismic active earth pressure coefficient for unsaturated soil (K_{aue}). Three-dimensional K_{aue} -surfaces are presented corresponding to three different Q's, namely, Q=–0.628 (infiltration), Q= 0 (no-flow), and Q=0.23 (evaporation). Regardless of the seismic forces and the backfill geometry, the K_{aue}-surfaces pertain to Q= 0 always lie between the infiltration and evaporation profiles. It is observed that K_{aue} enhances with the (a) decreases in i, and/or (b) increase in k_h. This enhancement of K_{aue} is more for infiltration, followed by hydrostatic and that followed by evaporation cases. It is also noticed that K_{aue} reduces as the magnitude of vertical seismic force enhances. This can be attributed to the fact (as mentioned in Shukla et al. 2009) that the application of upward-acting vertical seismic force curbs down the active earth pressure developed due to the action of k_h.

8.3.3.4 Impact of friction angle (ϕ') on K_{aue}

Fig. 8.17 shows the variation of K_{aue}, with soil friction angle, ϕ', corresponding to different climatic and seismic conditions. It can be observed that K_{aue} reduces with the improvement in frictional strength. The presence of seismic forces results in the further development of active earth pressure. Figs. 8.17a and 8.17b correspond to no-flow condition, Figs. 8.17c and 8.17d represent the effect of infiltration, and Figs. 8.17e and

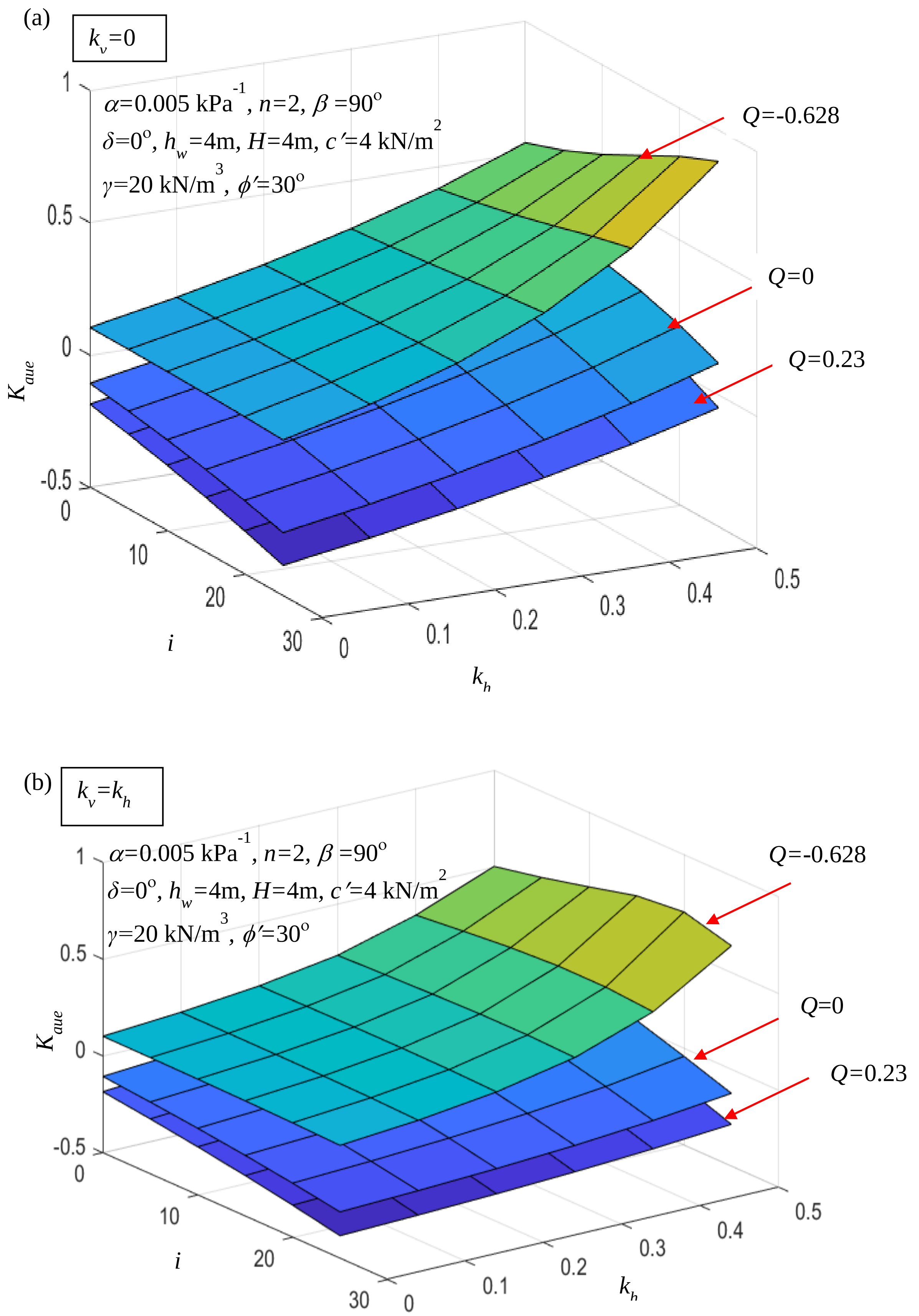

Fig. 8.16 The three-dimensional K_{aue}- k_h-i surfaces corresponding to three different flow ratios and two values of k_v : (a) k_v =0, and (b) $k_v = k_h$.

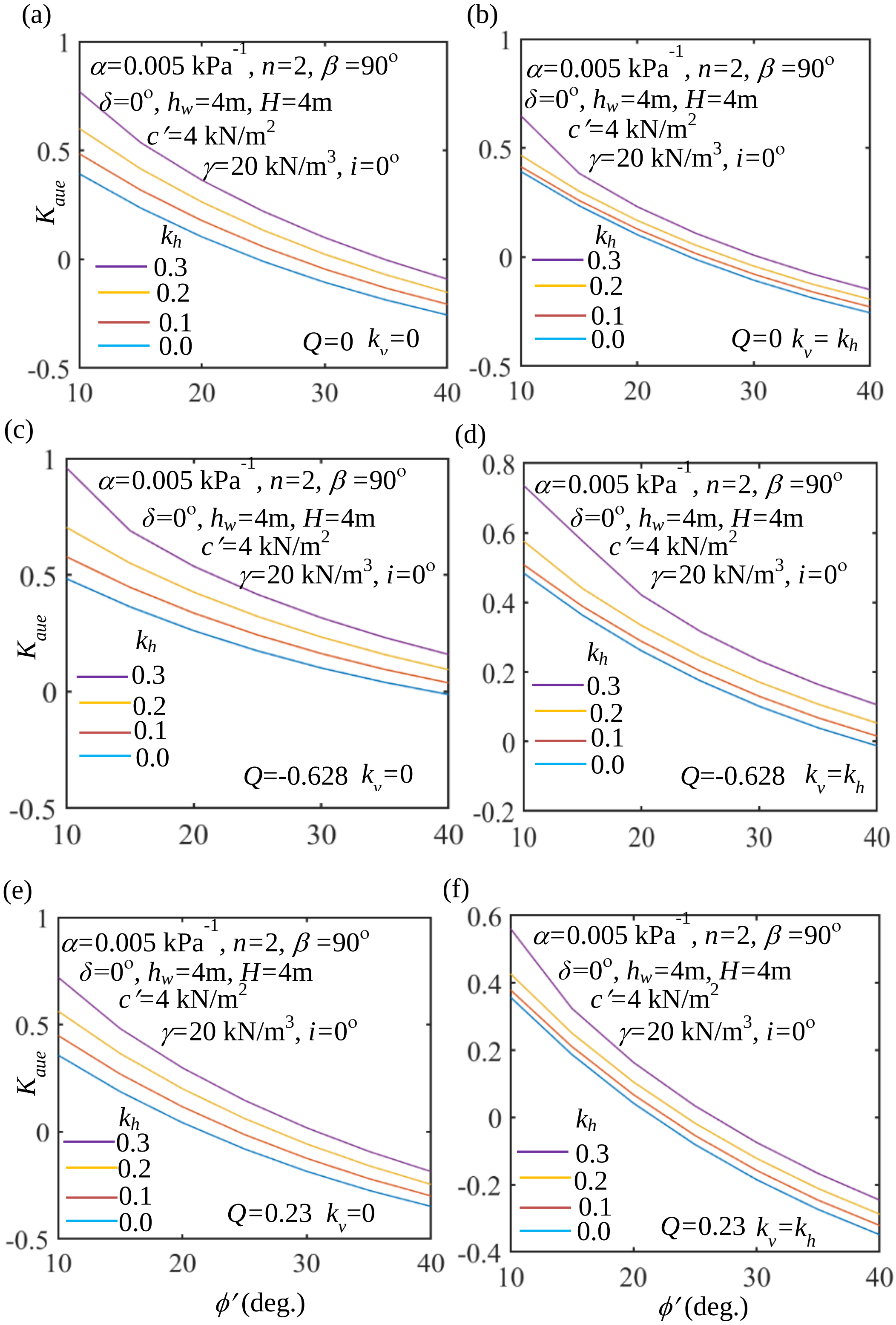

Fig. 8.17 The variation of K_{aue} with ϕ' corresponding to various flow ratios, namely, (a, b) Q=0 (c, d) Q=–0.628, and (e, f) Q=0.23 and subjected to different k_v: (a,c,e) k_v =0, and (b,d,f) $k_v = k_h$.

8.17f depict the effect of evaporative conditions. It can be seen that the decrement in the magnitude of K_{aue} is maximum for the evaporation condition and the least for the infiltrative condition. This can be interpreted as the fact that the vertical downward percolation in an unsaturated retained backfill increases the active earth pressure severely. The soil having high frictional strength seems to develop a negative value of K_{aue}. The negative value of K_{aue} indicates that the soil is in tension, and as a result, a tension crack may be generated. The manifestation of this negative K_{aue} appears to be higher when the water comes out of the soil surface.

8.3.3.5 Impact of wall inclination angle (β) on K_{aue}

Fig. 8.18 demonstrates how K_{aue} varies with wall inclination angle (β) under various climatic and seismic conditions. The investigation is carried out by choosing a very high range of β: 40°–120°. The figure shows that K_{aue} decreases as the magnitude of β enhances. Similar to the K_{aue}–ϕ' profiles, the bottom-most curves in all the graphs of K_{aue}–β profiles pertain to the non-seismic case. In the absence of vertical seismic force, the K_{aue}–β profiles appear to be parallel to each other, whereas when $k_v=k_h$, the K_{aue}–β curves diverge with the increase in the wall inclination. The addition of vertical seismic forces has a more severe effect on K_{aue} values. The decrement rate of K_{aue}–β curves appears to be maximum for evaporative flow and minimum for the infiltrative condition.

8.3.3.6 Impact of vG model parameters on K_{aue}

Figs. 8.19 and 8.20 present the effect of unsaturated properties (characterized by vG model parameters) on the active earth pressure coefficient**,** K_{aue}; Fig. 8.19 describes the impact of air-entry value, and Fig. 8.20 illustrates the impact of the

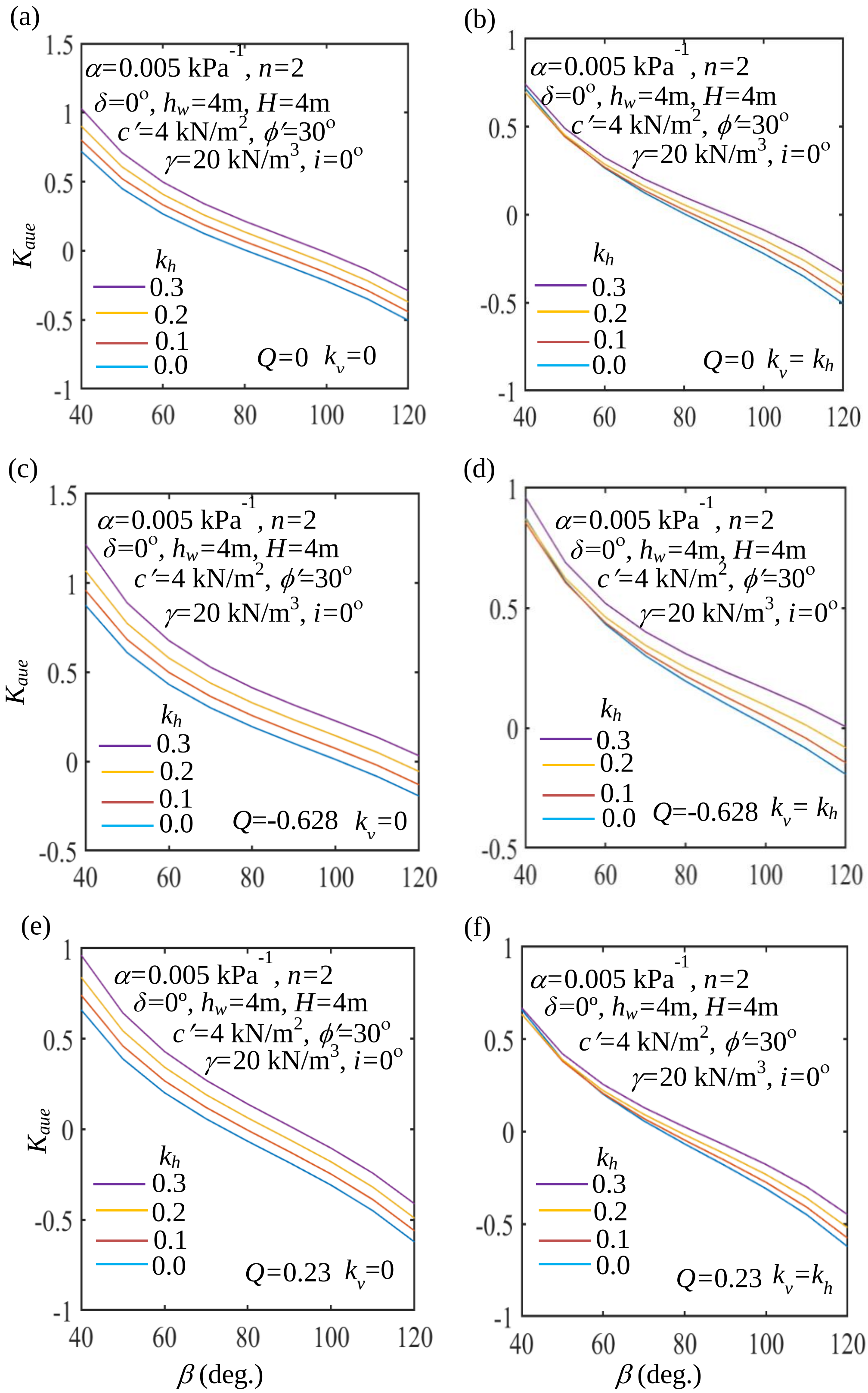

Fig. 8.18 The variation of K_{aue} with β corresponding to various flow ratios, namely, (a, b) Q=0 (c, d) Q=–0.628, and (e, f) Q=0.23 and subjected to different k_v: (a,c,e) k_v =0, and (b,d,f) k_v =k_h.

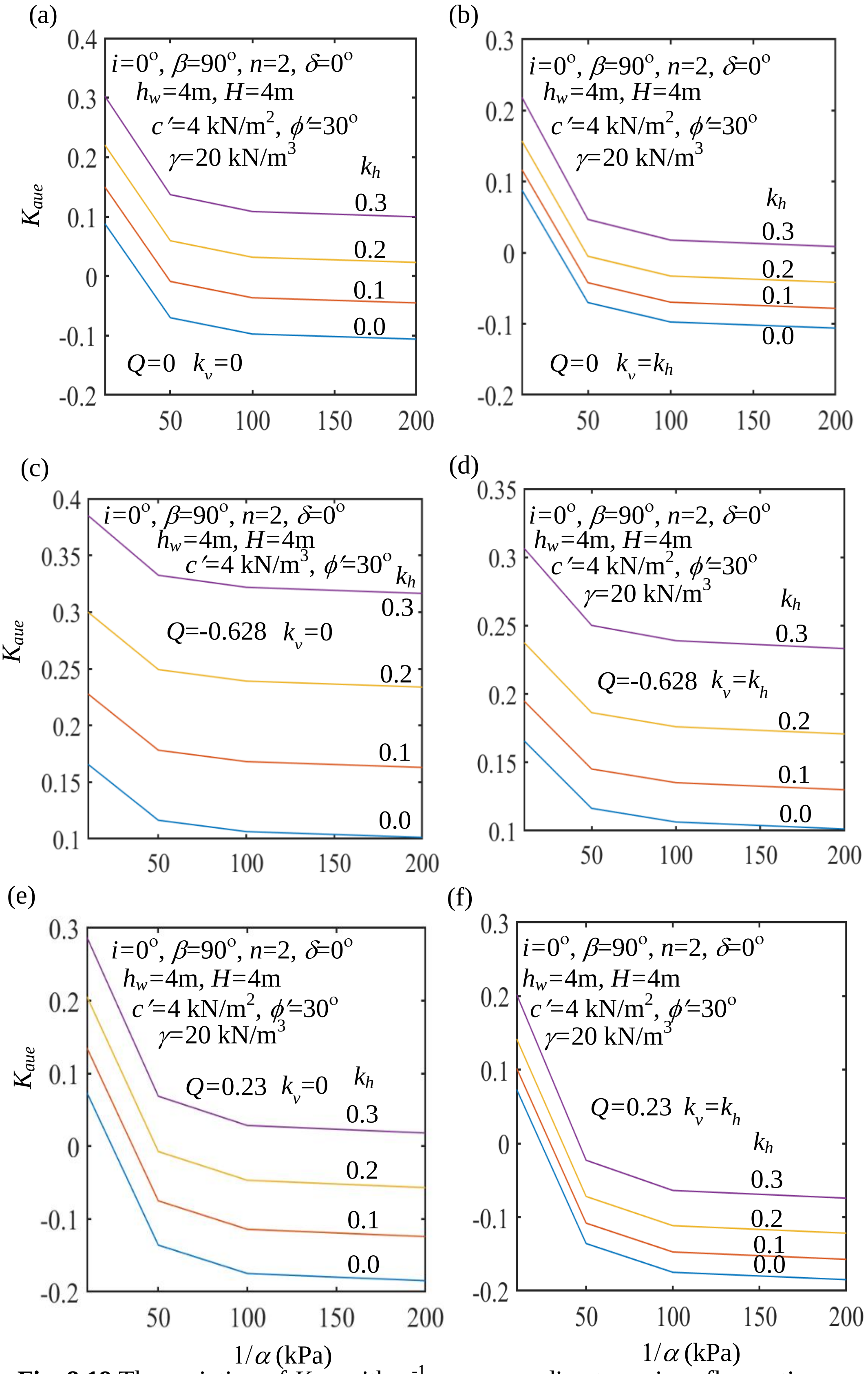

Fig. 8.19 The variation of K_{aue} with α^{-1} corresponding to various flow ratios, namely, (a, b) Q=0 (c, d) Q=–0.628, and (e, f) Q=0.23 and subjected to different k_v: (a,c,e) k_v =0, and (b,d,f) k_v =k_h.

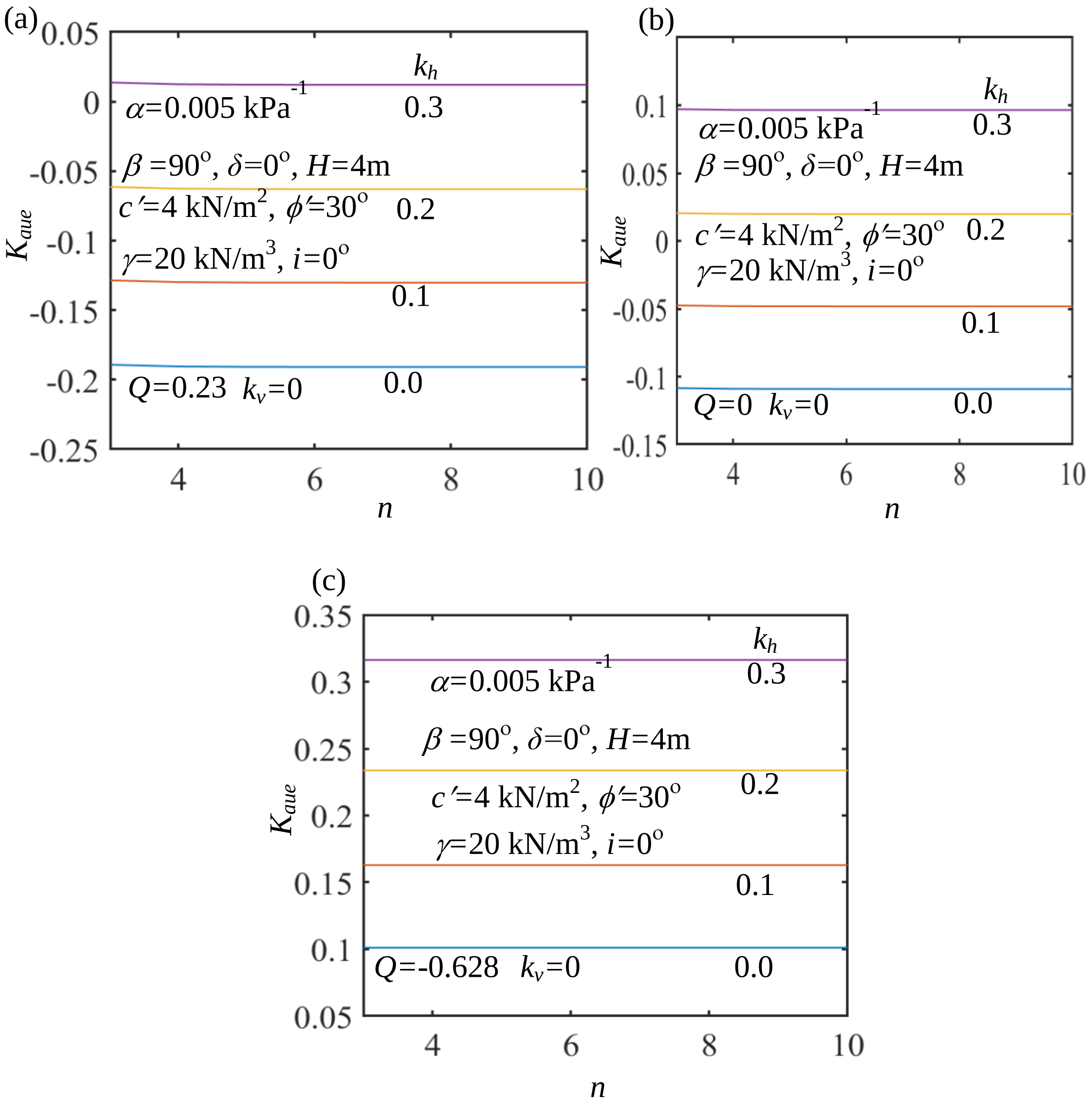

Fig. 8.20 The variation of K_{aue} with n considering various seismic loadings and corresponding to various flow ratios, namely, (a) Q=0.23, (b) Q=0, and (c) Q=–0.628.

pore spectrum parameter. The curves are plotted for three different flow ratios and different combinations of seismic forces. For a constant value of k_h, the K_{aue} profile decreases sharply with the increase in AEV up to a certain limit (say, $1/\alpha$=50 kPa); beyond that, a horizontal plateau is observed. It indicates that if the retained backfill is of coarse-grained type, the extent of the boundary effect zone appreciably influences the developed active earth pressures; nevertheless, for silty and other fine-grained soils, the K_{aue} profile appears to be unaffected by the onset of desaturation. The gap between the k_h -induced K_{aue} profile decreases as the vertical seismic force becomes active. Figs. 8.20a, 8.20b, and 8.20c depict the variation of K_{aue} with n corresponding to various flow conditions and different combinations of seismic forces. The figure manifests that there is no significant changes in the magnitude K_{aue} as n value increases. The detrimental effect of the infiltration process and the applied seismic forces are visible even in this figure.

8.3.3.7 Impact of water table depth (h_w) on K_{aue}

Fig. 8.21 illustrates the effect of groundwater table fluctuation on the computed K_{aue} conforming to different flow conditions and different seismic force combinations. With the lowering of GWT the extent of vadose zone increases resulting in the reduction of the active earth pressure. This is manifested by the decreasing trend of the $K_{aue} - h_w$ profiles. Beyond a certain h_w, K_{aue} starts to become negative. The negative value of K_{aue} happens to be significantly higher for the evaporative flow under the static loading. The $K_{aue} - h_w$ curve corresponding to k_h=0.3 remains to be the topmost curve indicating the higher value of AEP due to the application of the horizontal seismic force. The upwardly directed vertical seismic force however, lowers the magnitude of earth pressure.

8.3.3.8 Impact of δ on K_{aue}

Fig. 8.22 demonstrates the effect of footing roughness (δ) on K_{aue} for different flow conditions and seismicity. For vertically upward steady-state flow, the influence of δ seems to be effective only for the static loading; with the increase in horizontal seismic force the K_{aue} -δ curves appear to be horizontal. The same feature is observed for the hydrostatic condition. When water percolates within the vadose zone, the K_{aue} -δ

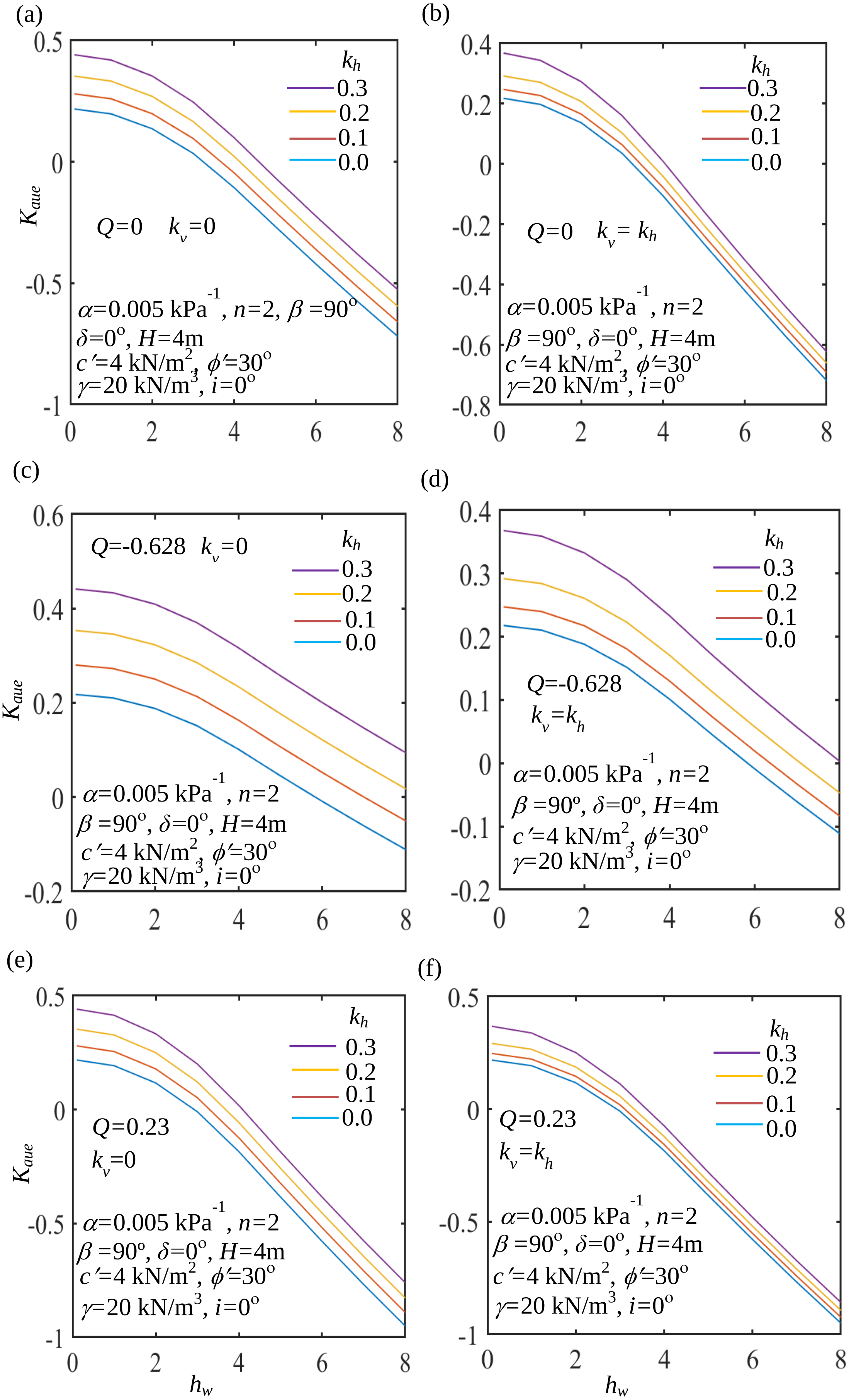

Fig. 8.21 The variation of K_{aue} with h_w corresponding to various flow ratios, namely, (a, b) Q=0 (c, d) Q=–0.628, and (e, f) Q=0.23 and subjected to different k_v: (a,c,e) k_v =0, and (b,d,f) k_v =k_h.

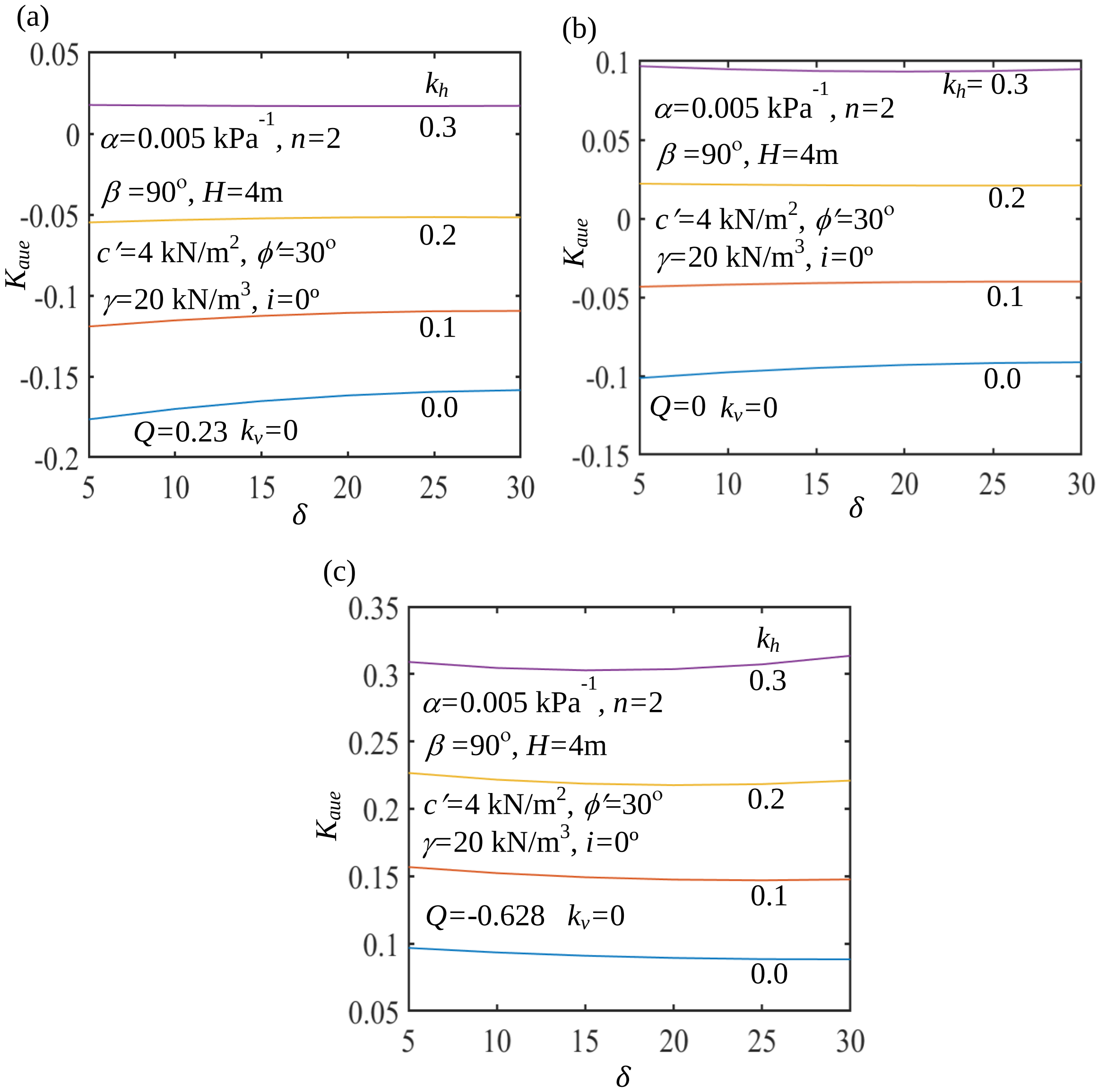

Fig. 8.22 The variation of K_{aue} with δ considering various seismic loadings and corresponding to various flow ratios, namely, (a) Q=0.23, (b) Q=0, and (c) Q=–0.628.

profiles behave bit differently; initially, the curves decrease a bit and afterwards exhibit a slight increasing trend. For the chosen parameters, the infiltration-induced K_{aue} -δ profiles remain in positive zone, even for the static loading. On the other hand, except the curve corresponding to k_h =0.3, all other curves pertain to the evaporative flow falls in the negative zone. Overall, the influence of δ seems to be marginal on the computed K_{aue} values, as compare to the other parameters.

8.3.3.9 Failure surfaces

Fig. 8.23 presents the extent of the failure triangular wedges by varying different input parameters; Figs. 8.23a-8.23c represent the failure pattern for vertical smooth wall with horizontal backfilled soil experiencing different flow patterns and different level of seismic activities, whereas Figs. 8.23d-8.23f display the effect of wall inclination and backfill inclination for no-flow condition. For all the plotted figures, k_v =0. At the failure state, the following three observations are noted: (a) the soil volume encompassed within the planar failure surface grows in size with the increase in k_h value, (b) failure zone volume appear to be maximum for infiltration and minimum for evaporation, and (c) the k_h factor seems to be highly dominating on the developed failure surfaces if water percolates in vertically downward direction. Comparing Fig. 8.23a and 8.23d, it can be inferred that the enclosed soil zone within the plastic failure surface inflates as the retaining wall and the backfill surfaces become inclined. Fig. 8.23e shows the effect of wall inclination on the same backfilled soils (i=10°), while Fig. 8.23f displays the visual impact of the failure surfaces developed behind a retaining wall (β=80°), with varying inclination angles. With the increase in β, the soil volume within the sliding surface decreases.

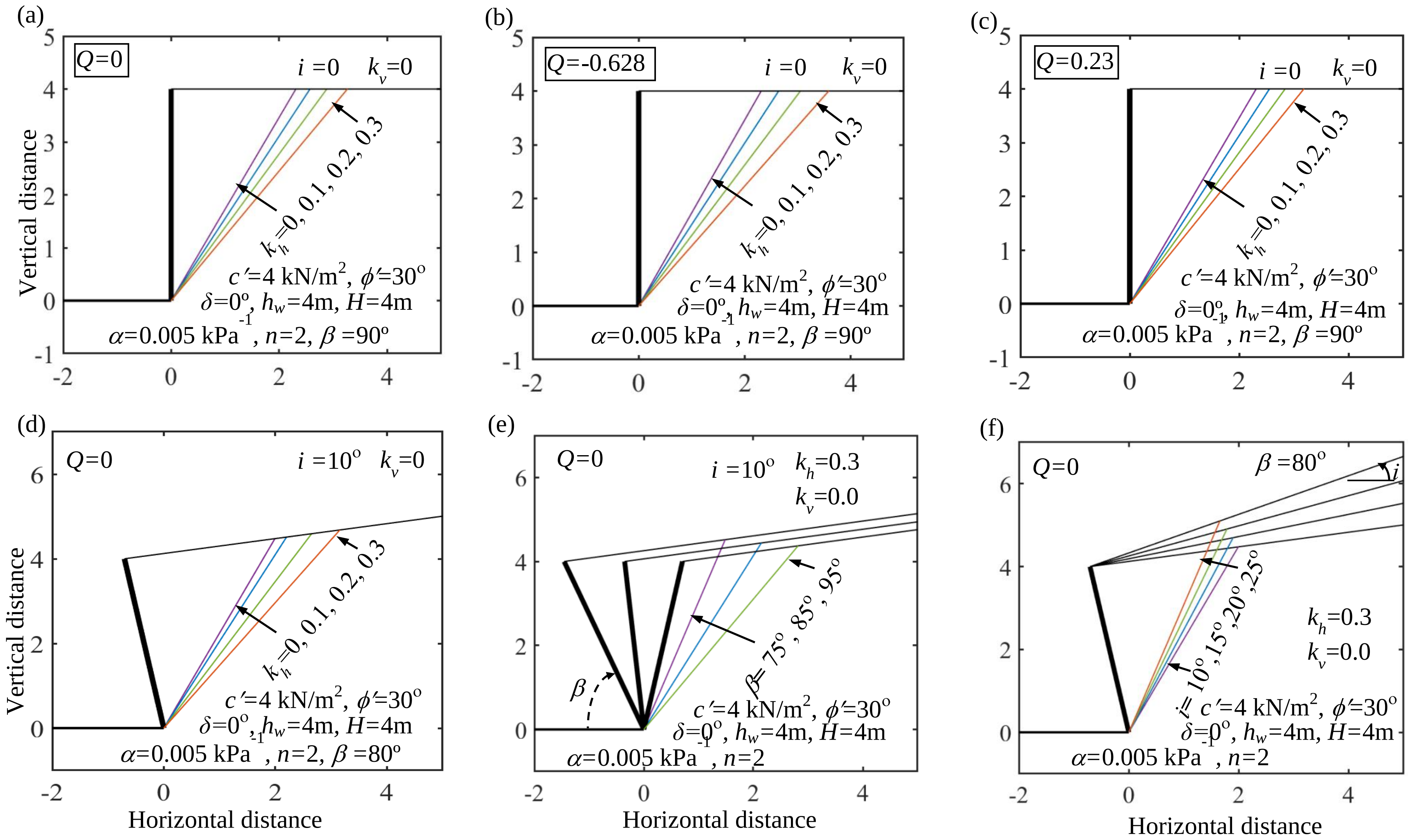

Fig. 8.23 The spread of planar failure surfaces considering various seismic loadings and corresponding to (a-c) vertical wall supporting horizontal backfills and (d-f) inclined wall holding the slopy backfill.

8.3.4 Verification

Fig. 8.24 depicts the comparison of the magnitudes of K_{aue} obtained from the present study with the solutions reported by Rajesh and Ganesh (2022) for different k_h and β values. Rajesh and Ganesh (2022) considered the ground surface of backfill is horizontal. As a result, in order to compare the computed solutions with Rajesh and Ganesh (2022), the backfill is assumed as horizontal. The comparison is carried out for sandy soil (c'=0 kPa and ϕ'=30°) and the flow condition is considered as hydrostatic. The vG parameters are fixed at α=0.1 kPa^{-1} and n=5 and the wall-interface angle δ is kept as δ = (2/3)*ϕ. The magnitude of k_v is taken account as $k_v = -0.5k_h$. The negative value of k_v indicates the direction of vertical seismic force is downward that was prescribed in the work of Rajesh and Ganesh (2022). It can be observed that the present solutions match quite well with the available results of Rajesh and Ganesh (2022).

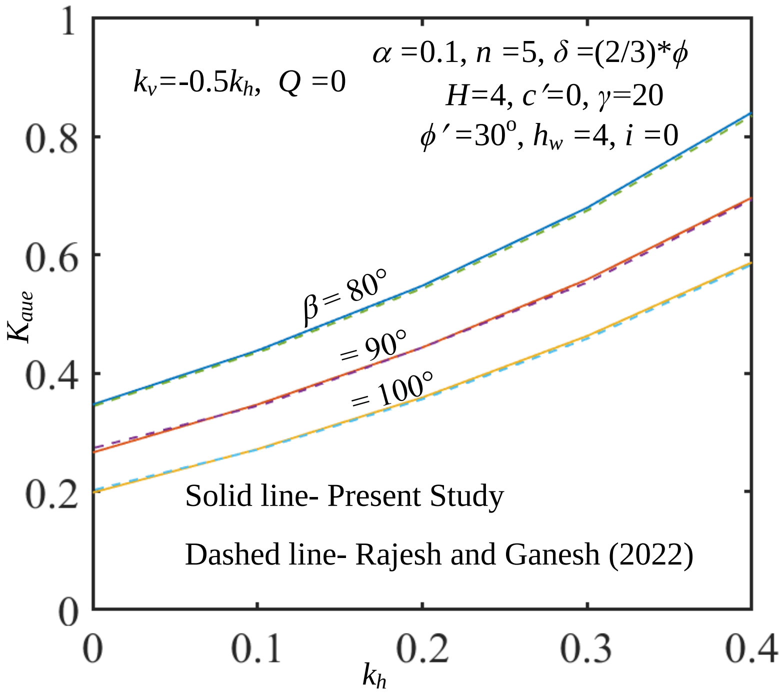

Fig. 8.24 The comparison between the present solutions with the solutions reported by Rajesh and Ganesh (2022).

8.4 SUMMARY

In this chapter, the earth-pressure coefficients of unsaturated retaining soils are determined by duly incorporating the matric suction effect. Due to its flexibility and wider applicability in the stability analysis, the suction-stress-based effective stress formulations are employed in the present computation. Unlike the conventional practices, the asymmetry fitting parameter of the SWCC curve is not forced to have a strict value on the basis of the pore spectrum number. By relaxing the constraint on the SWCC parameter, the Rankine's earth pressure coefficients are obtained for the rest, active, and passive states. The tensile crack depths are also evaluated. The simulations are carried out for hydrostatic, infiltration, as well as evaporation. The independence of the SWCC parameters exhibits marked influences during the drying of the vadose zone having high air entry value and non-uniform pore distribution. An attempt has also been made to incorporate the two parameter dependent permeability models. The entire exercise establishes the fact that although the independence of the residual-state-controlling-parameter is highly required for modeling the real field scenario, however, traditional one-parameter permeability model is quite efficient and reliable in retaining wall analysis.

The second segment of this chapter involves the computation of active earth pressure generated behind an inclined retaining wall supporting inclined unsaturated backfill under seismic conditions. Extensive numerical simulations are carried out to understand how and to what extent the active pressure coefficient gets influenced by the wall inclination, backfill slope angle, backfill soil properties (mechanical strength, unsaturated properties), groundwater table fluctuations, steady-flow characteristics, seismic acceleration coefficients, and soil-wall roughness conditions. A series of design charts are prepared. These charts might be helpful to the practicing engineers in developing an understanding of retaining walls used to support sloped backfills in arid and semi-arid zones, particularly in areas susceptible to seismic forces.

8.5 LIMITATIONS

In this chapter, the soil backfill is considered as homogeneous and isotropic, which may not accurately represent real-world soil conditions where variations in composition and structure are common. It is also assumed that the retaining wall is rigid and does not deform. In reality, retaining walls often experience deformations, and considering wall flexibility can affect the accuracy of predictions. Moreover, it is considered that the fluid pressure and the flow rate inside and outside the tension cracks are the same. This means that the change in suction locally around the crack is ignored. Furthermore, the spatial perspective is prioritized in evaluating suction stress variation, while the temporal aspect is ignored. A series of design charts are presented by considering specified parametric variations. If the necessary field conditions extend beyond the prescribed ranges, the determination of the lateral earth pressures can be effortlessly achieved by employing the provided formulations.